Monthly Notices
of the
ROYAL ASTRONOMICAL SOCIETY

MNRAS **493,** 3194–3211 (2020)
Advance Access publication 2020 February 10

doi:10.1093/mnras/staa355

The redshift evolution of rest-UV spectroscopic properties to $z \sim 5$

Anthony J. Pahl [1]★ Alice Shapley,[1] Andreas L. Faisst,[2] Peter L. Capak,[2] Xinnan Du,[3] Naveen A. Reddy,[3] Peter Laursen[4,5] and Michael W. Topping[1]

[1]*Department of Physics and Astronomy, University of California, Los Angeles, CA 90095, USA*
[2]*IPAC, California Institute of Technology, 1200 East California Boulevard, Pasadena, CA 91125, USA*
[3]*Department of Physics and Astronomy, University of California Riverside, Riverside, CA 92521, USA*
[4]*Institute of Theoretical Astrophysics, University of Oslo, PO Box 1029, Blindern, 0315 Oslo, Norway*
[5]*Cosmic Dawn Center (DAWN), Niels Bohr Institute, University of Copenhagen, Vibenshuset, Lyngbyvej 2, DK-2100 Copenhagen Ø, Denmark*

Accepted 2020 January 30. Received 2020 January 16; in original form 2019 October 9

ABSTRACT

We perform a comprehensive analysis of the redshift evolution of the rest-UV spectra of star-forming galaxies out to $z \sim 5$. We combine new $z \sim 5$ measurements of H I Ly α and low- and high-ionization interstellar metal absorption features with comparable measurements at $z \sim 2$–4. We measure the equivalent widths of interstellar absorption features using stacked spectra in bins of Ly α equivalent width, performing corrections to Ly α strengths based on a model for the transmission of the intergalactic medium. We find a strong correlation between decreasing low-ionization absorption strength and increasing Ly α emission strength over the redshift range $z \sim 2$–5, suggesting that both of these quantities are fundamentally linked to neutral gas covering fraction. At the highest Ly α equivalent widths, we observe evolution at $z \sim 5$ towards greater Ly α emission strength at fixed low-ionization absorption strength. If we interpret the non-evolving relationship of Ly α emission strength and low-ionization line strength at $z \sim 2-4$ as primarily reflecting the radiative transfer of Ly α photons, this evolution at $z \sim 5$ suggests a higher intrinsic production rate of Ly α photons than at lower redshift. Our conclusion is supported by the joint evolution of the relationships among Ly α emission strength, interstellar absorption strength, and dust reddening. We perform additional analysis in bins of stellar mass, star formation rate, UV luminosity, and age, examining how the relationships between galaxy properties and Ly α emission evolve towards higher redshift. We conclude that increasing intrinsic Ly α photon production and strong detection of nebular C IV emission (signalling lower metallicity) at $z \sim 5$ indicate an elevated ionized photon production efficiency ($\xi_{\rm ion}$).

Key words: galaxies: evolution – galaxies: high-redshift – galaxies: ISM.

1 INTRODUCTION

The rest-UV spectrum of a star-forming galaxy provides a uniquely rich probe of the properties of massive stars and the interstellar and circumgalactic medium (ISM and CGM; Shapley et al. 2003; Steidel et al. 2010, 2016; Leitherer et al. 2011; Senchyna et al. 2019). Understanding the interplay between these components is important for placing constraints on galaxy evolution across cosmic time. Furthermore, the gas in and around distant galaxies that is probed by rest-UV spectra also modulates the escape of ionization radiation. This gas provides important clues to the process of cosmic reionization, a key phase transition in which the intergalactic medium (IGM) transformed from neutral to ionized by roughly a billion years after the big bang at $z \sim 6$ (Fan, Carilli & Keating 2006; Robertson et al. 2015; Planck Collaboration et al. 2016).

Measuring the rest-UV spectra of distant galaxies requires optical instrumentation and long integrations. Based on observations with instruments such as the Low Resolution Imager and Spectrometer (LRIS) on the Keck I Telescope (Oke et al. 1995; Steidel et al. 2004), there have been several analyses of the relationships between rest-UV spectral features and other galaxy properties out to $z \sim 4$ (e.g. Jones, Stark & Ellis 2012; Du et al. 2018; Marchi et al. 2019). Du et al. (2018) (hereafter, D18) performed a comprehensive evolutionary analysis of rest-UV spectral trends of star-forming galaxies from $z \sim 2$–4. This analysis centred around the hydrogen Ly α line and low- and high-ionization interstellar (LIS and HIS) metal absorption lines, which together probe the neutral gas covering fraction, gas kinematics, and ISM and CGM properties of galaxies. Both D18

★ E-mail: pahl@astro.ucla.edu

and Jones et al. (2012) find a strong and non-evolving correlation between Ly α equivalent width (EW) and low-ionization interstellar absorption EW, revealing the connection between escaping Ly α photons (and, by extension, ionizing radiation; Reddy et al. 2016; Chisholm et al. 2018; Steidel et al. 2018) and the covering fraction of neutral gas in the CGM. Building on these earlier works, we now seek to probe the rest-UV properties of galaxies at redshifts even closer to the epoch of reionization.

Approaching reionization at $z > 6$, we must attempt to understand how the rest-UV spectrum reveals the changing properties of both massive stars and the ISM/CGM at higher redshift. The evolution of the relationship between Ly α emission strength and LIS absorption strength sheds light on the intrinsic production rate of Ly α photons in high-redshift galaxies, which in turn probes the intrinsic ionizing-photon production rate. Affecting observations near reionization, the IGM becomes more optically thick to Ly α photons and attenuates the spectra of galaxies. We must correct for this attenuation to accurately determine the changing intrinsic production rate of Ly α photons. As stated in D18, the Ly α–LIS relationship also indicates the changing covering fraction of neutral gas in the CGM at higher redshift. Both intrinsic ionizing-photon production rate and neutral-gas covering fraction are key components of understanding the contribution of star-forming galaxies to the ionizing background during reionization (Robertson et al. 2015; Chisholm et al. 2018, 2019; Nakajima et al. 2018; Steidel et al. 2018; Trainor et al. 2019).

The DEIMOS 10K Spectroscopic Survey (Hasinger et al. 2018) provides an ideal data set for performing this type of analysis, including thousands of galaxies ranging from $z \sim 0$ to $z \sim 6$ with deep, rest-UV spectroscopy. This survey was conducted in the COSMOS field (Scoville et al. 2007), which is covered by extensive broad-band photometry enabling the measurement of integrated galaxy properties. In this work, we extend the analysis of D18 to higher redshift by carefully examining a $z \sim 5$ sample of star-forming galaxies drawn from the DEIMOS 10K Spectroscopic Survey. We perform a joint analysis of the new $z \sim 5$ sample with the $z \sim 2$–4 samples of D18, using consistent methodology across all redshifts to remove any potential systematics.

In Section 2, we introduce our sample of $z \sim 5$ galaxies and the $z \sim 2$–4 galaxies of D18, and discuss sample completeness, redshift measurements, and spectral energy distribution (SED) fitting. In Section 3, we describe the methodology for measuring the EWs of Ly α and interstellar absorption features, and the binning of the sample and subsequent creation of composite spectra. In Section 4, we present the resulting trends of rest-UV spectral features at $z \sim 5$. In Section 5 we analyse the sample at a finer redshift sampling and discuss the implications of our results for quantifying the changing intrinsic Ly α photon production and the contribution of star-forming galaxies to reionization. In Section 6, we summarize our key results and conclude.

Throughout this paper, we adopt a standard Λ cold dark matter cosmology with $\Omega_m = 0.3$, $\Omega_\Lambda = 0.7$, and $H_0 = 70$ km s^{-1} Mpc^{-1}.

2 SAMPLE

2.1 Selection criteria

We analysed a sample of galaxies drawn from the DEIMOS 10K Spectroscopic Survey of the COSMOS field (Scoville et al. 2007; Hasinger et al. 2018). This survey provides deep optical spectroscopy taken with the DEep Imaging Multi-Object Spectrograph (DEIMOS) on the Keck II telescope on Mauna Kea. The COSMOS field is covered by a wealth of ancillary data, including multiwavelength imaging from space-based and ground-based missions. Out of the ∼10 000 galaxies targeted in the DEIMOS 10K survey, we selected those identified as Lyman break galaxies (LBGs), dropping out in the B_J and g^+ optical filters for $z \sim 4$, and V_J or r^+ for $z \sim 5$. Also included were objects with photometric redshifts between $z \sim 3.75$ and 5.75. These criteria yielded a parent sample of 416 star-forming galaxies at high-redshift, 337 selected via dropout and 79 via photometric redshifts.

We further required objects to have high-confidence spectroscopically confirmed redshifts. The DEIMOS 10K catalogue provided a quality flag *Qg* indicating the confidence level of the spectroscopic-redshift measurement based on the quality of the spectrum and the number of features in the redshift estimate (either Ly α or LIS lines). We examined all objects with $Qg \geq 1$ that satisfied the above photometric criteria, eliminating only those with unsuccessful redshift measurements. From this set of objects, we measured a redshift from the Ly α line, LIS lines, or both. We successfully recovered redshifts for 196 objects at $4 < z < 5.5$. For the purpose of our completeness calculations, from our parent photometric sample of 416 galaxies, we removed galaxies selected by photometric redshift that had measured spectroscopic redshifts $z < 4.0$, reducing the parent sample to 375.

2.2 Systemic redshifts

Ideally, rest-optical nebular emission lines would be used to estimate the systemic redshifts of high-redshift galaxies. As these lines are shifted into the thermal infrared at $z \sim 5$, we measure the redshifts of the spectra via the redshifts of the Ly α emission line ($z_{\mathrm{Ly}\alpha}$) and the three strongest LIS absorption features (z_{LIS}): Si II λ1260, O I λ1302 + Si II λ1304, and C II λ1334. Using the spectroscopic redshifts provided by DEIMOS 10K, we estimated the central wavelength of each non-resonant line and fit a Gaussian profile to the flux-calibrated spectrum. Each line was visually inspected to confirm the validity of the line detection and corresponding fit. The redshifts based on the central wavelengths of the well-fitted Gaussian profiles of the three LIS lines were averaged with weights to calculate z_{LIS}. Given the asymmetry of the Ly α profile, we did not model it with a Gaussian, but rather calculated $z_{\mathrm{Ly}\alpha}$ based on the wavelength at which the spectrum reached a maximum within the Ly α profile. We then determined the systemic redshift using the method described in Rudie et al. (2012). $z_{\mathrm{Ly}\alpha}$ was assumed to be offset from systemic by 300 km s^{-1} and z_{LIS} by −160 km s^{-1}, with these offsets empirically determined by Steidel et al. (2010). While these rules are calculated at $z \sim 2$, we assume they hold to $z \sim 5$ in the absence of other information. This calculation enabled an estimate of the systemic redshift based on a high-quality measurement of either $z_{\mathrm{Ly}\alpha}$ or z_{LIS}. If both $z_{\mathrm{Ly}\alpha}$ and z_{LIS} were measured, the systemic redshift was estimated as the average of the two. After combining 14 duplicate spectra, removing four spectra with poorly fit lines and two spectra with background subtraction issues, we assembled a final sample of 176 objects between $4 < z < 5.5$: 68 with $z_{\mathrm{Ly}\alpha}$ only, 34 with z_{LIS} only, and 74 with both types of redshift measurement. The redshift distribution of the sample is displayed in Fig. 1. The median redshift of our sample is $z_{\mathrm{med}} = 4.521$, with a 16th–84th percentile range of 4.172–4.930. The redshift uncertainty σ_z for each object was calculated using uncertainties on the assumed velocity offsets of Ly α and LIS, empirically determined in Steidel et al. (2010). For galaxies with both $z_{\mathrm{Ly}\alpha}$ and z_{LIS} measured, we assumed $\sigma_{v_{\mathrm{Ly}\alpha}} = 175$ km s^{-1} and $\sigma_{v_{\mathrm{LIS}}} = 115$ km s^{-1}. For galaxies with only z_{LIS} measured,

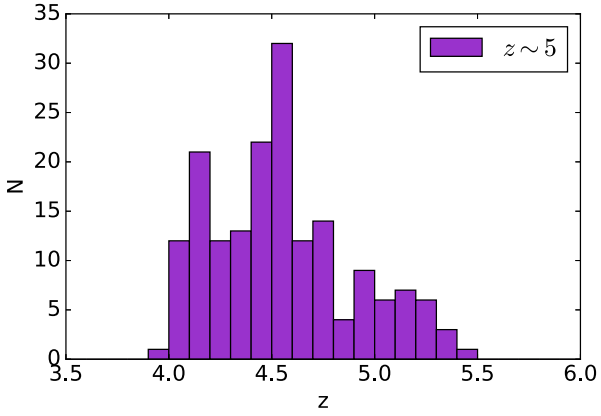

Figure 1. Redshift distribution of the DEIMOS 10K sample at $z \sim 5$. The sample comprises 176 objects with a median redshift of 4.521.

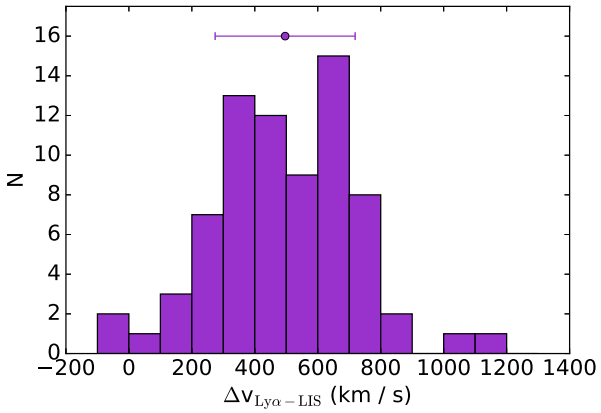

Figure 2. Distribution of velocity offsets between Lyα emission and LIS absorption. The velocities are distributed about $\langle \Delta v_{\mathrm{Ly}\alpha\text{–LIS}} \rangle = 496 \pm 222$ km s^{-1}.

we assumed $\sigma_{v_{\mathrm{LIS}}} = 165$ km s^{-1}. For galaxies with only $z_{\mathrm{Ly}\alpha}$ measured, we assumed $\sigma_{v_{\mathrm{Ly}\alpha}} = 175$ km s^{-1}. The median σ_z of the sample redshifts was 0.002. We refer to this sample as the '$z \sim 5$ sample' for simplicity and keep this sample distinct from samples featured in D18 to signify a new data set.

For the objects with both Lyα and LIS absorption redshifts measured, we examined the distribution of velocity differences between Lyα and LIS lines in Fig. 2. This measurement was calculated as

$$\Delta v_{\mathrm{Ly}\alpha\text{–LIS}} = c \times \frac{(z_{\mathrm{Ly}\alpha} - z_{\mathrm{LIS}})}{(1 + (z_{\mathrm{Ly}\alpha} + z_{\mathrm{LIS}})/2)}. \quad (1)$$

The velocity differences are distributed about a $\langle \Delta v_{\mathrm{Ly}\alpha\text{–LIS}} \rangle = 496$ km s^{-1} with a standard deviation of 222 km s^{-1}. This value is largely consistent with $\langle \Delta v_{\mathrm{Ly}\alpha\text{–LIS}} \rangle \sim 600$ km s^{-1} of Steidel et al. (2010) at $z \sim 2$–3, and $\langle \Delta v_{\mathrm{Ly}\alpha\text{–LIS}} \rangle = 429 \pm 229$ km s^{-1} of Faisst et al. (2016) at $z \sim 5$, the latter using a similar sample drawn from the DEIMOS 10K survey. The distribution of velocity differences of Fig. 2 has a similar shape to that of $z \sim 3$ LBGs of Shapley et al. (2003), a sample which has been shown to have similar outflow kinematics to those of the Steidel et al. (2010) $z \sim 2$ sample. This similarity lends credence to our assumption that the outflow velocities calculated at $z \sim 2$ are applicable out to $z \sim 5$.

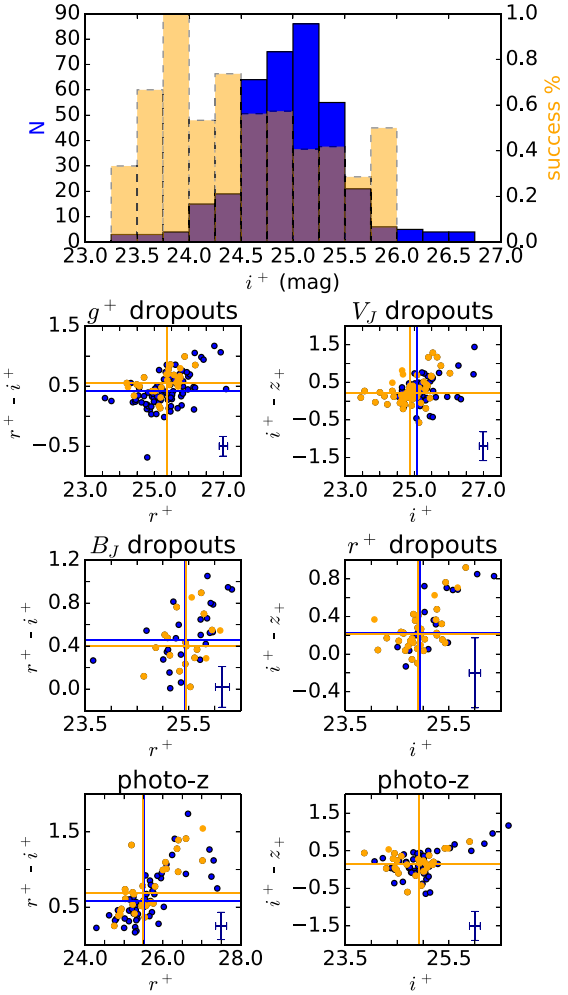

Figure 3. Completeness of the $z \sim 5$ sample. *Top panel:* Histogram (in orange) showing the percentage of successfully measuring a high-confidence spectroscopic redshift in the $z \sim 5$ parent sample as a function of i^+ magnitude. The total i^+ magnitude distribution of the parent sample is overplotted in blue. The completeness drops below ∼60 per cent at an i^+ magnitude of ∼25.0. *Middle four panels:* Colour–magnitude diagrams of the dropout-selected galaxies. The parent sample is plotted in blue, with the corresponding median colours and magnitudes plotted as vertical and horizontal lines. The $z \sim 5$ sample with well-measured redshifts is plotted in orange, along with the corresponding medians. Typical error bars for the respective samples are given in the lower-right corner of each panel. No significant deviation between the parent sample and the spectroscopic sample is found in colour–magnitude space. *Bottom two panels:* Colour–magnitude diagrams of the galaxies selected by photometric redshifts between $3.75 < z < 5.75$. These panels follow the same colour scheme as the dropout-selected galaxy panels.

2.3 Completeness

In order to explore the completeness of the $z \sim 5$ COSMOS DEIMOS sample, we examined the number of galaxies in the parent sample that report a high-confidence redshift as a function of brightness. The results of this analysis are illustrated in the top panel of Fig. 3, where the total number of galaxies in the parent sample and thepercentage of successful redshift measurements are plotted as a function of i^+-band magnitude. At $i^+ > 25$ mag, the sample completeness drops below ∼60 per cent, thus a more careful examination of the sample completeness must be performed.

As described above, spectroscopic redshifts at high redshift are measured using a combination of H I Lyα emission and LIS absorption lines of Si II λ1260, O I λ1302 + Si II λ1304, and C II λ1334. Measuring redshifts requires the robust detections of these lines. Since we explore the *variation* of the strengths of LIS and HIS absorption as a function of Lyα emission strength, strong detections should not bias our results. It is more important to examine whether the galaxies in our $z \sim 5$ spectroscopic sample are representative of the parent photometric sample of star-forming galaxies in terms of other galaxy properties, such as colour and brightness. To investigate this issue, we plotted our sample and the parent photometric sample in colour–magnitude space in the bottom panels of Fig. 3. For the galaxies selected as dropouts, all filters chosen in the colour−magnitude diagram are redward of the corresponding dropout filter. For both dropouts and photo-z selected samples, all but two of the deviations in median colour are smaller than 0.06 mag, and all but one of the deviations in median magnitude are smaller than 0.05 mag. The lack of significant deviation in the median between our sample and the parent photometric sample demonstrates that the sample is not significantly biased in colour and brightness. The most significant deviation (0.22 mag) is between the median i^+-band magnitudes of the V_J dropouts in our sample versus the parent sample, thus we examined our sample as a function of brightness in detail in Section 3.1. We conclude that our spectroscopic sample is not significantly biased towards certain types of star-forming galaxies with respect to the parent photometric sample in the same redshift range.

2.4 $z \sim 2$–4 sample

For a lower-redshift comparison sample, we used the $z \sim 2$–4 LBGs described in D18. The sample consists of $z \sim 2$–3 galaxies preselected using U_nGR colour cuts and followed up with LRIS on Keck I as part of the redshift surveys described in Steidel et al. (2003), Steidel et al. (2004), and Reddy et al. (2008). The $z \sim 4$ sample was drawn from Jones et al. (2012) and consists of B-band dropouts in the GOODS-S field, 42 of which were followed up with DEIMOS on Keck II. In addition, 28 had spectra from the FOcal Reducer and low-dispersion Spectograph 2 (FORS2; Vanzella et al. 2005, 2006, 2008, 2009) archival catalogue. The average spectral resolutions were $R_{\rm average} \sim 970$ and 1280 for the $z \sim 2$–3 and $z \sim 4$ samples, respectively, compared to $R_{\rm average} \sim 2700$ for the $z \sim 5$ sample. Systemic redshifts were measured in a similar method to that described above,[1] and the sample was divided into three bins of increasing redshift, with 671 $z \sim 2$ objects defined at $1.4 \leq z < 2.7$, 352 $z \sim 3$ objects at $2.7 \leq z < 3.4$, and 80 $z \sim 4$ objects at $3.4 \leq z \leq 4.5$. The full redshift distribution of the $z \sim 2$–5 galaxies is displayed in Fig. 4. Some overlap does exist between galaxies in the $z \sim 4$ and $z \sim 5$ samples, but they are largely distinct with median redshifts of 3.856 and 4.521, respectively. In Section 5, we search for evolution within the $z \sim 5$ sample by dividing this sample into two distinct redshift bins with $z_{\rm med} = 4.330$ and 4.742. We note that the latter of these two more finely sampled bins does not overlap in redshift space with the $z \sim 4$ sample from Jones et al. (2012).

[1]There was a small difference in the method for estimating systemic redshifts in the case where both $z_{{\rm Ly}\alpha}$ and $z_{\rm LIS}$ were measured. D18 simply used $z_{{\rm Ly}\alpha}$ with an assumed velocity offset instead of averaging the two redshift measurements. In practice, the two estimates are very similar and this small difference in approach does not affect our results.

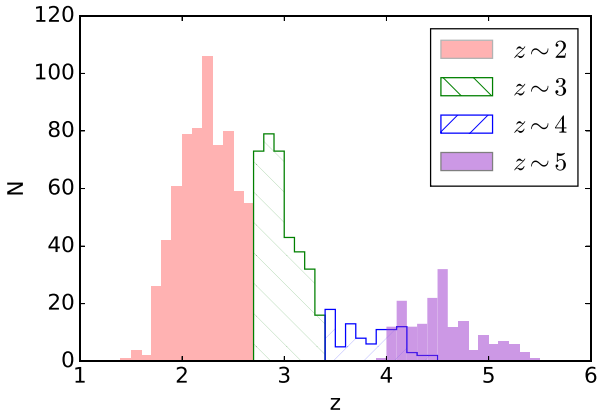

Figure 4. Redshift distribution of the four samples at $z \sim 2$–5. The $z \sim 2$, 3, and 4 samples in red, green, and blue are drawn from D18. The $z \sim 5$ sample from this work is shown in purple.

2.5 SED fits

As we aim to compare spectral trends across a range of redshifts, we wanted to make a controlled comparison between similar types of galaxies at each redshift. To this end, we first made measurements of the galaxy stellar-population properties in each redshift bin via stellar-population synthesis model fits to the galaxy SEDs. We used photometry from the publicly available catalogues of COSMOS2015 (Laigle et al. 2016) for 171 of our objects, well matched in RA and Dec., and, for four objects, we used the photometric catalogue of Capak et al. (2007). For one object, we used the COSMOS Intermediate and Broad Band Photometry Catalogue 2008 (Capak et al. 2008)[2], but, as this object did not have sufficient coverage redward of the Balmer break, we removed it from the sample, leaving us with 175 galaxies at $z \sim 5$.

In our SED fitting, we utilized the Bruzual and Charlot (2003) stellar-population templates and assumed a Chabrier (2003) initial mass function (IMF). As these models do not include emission lines, we omitted the IRAC channel 1 band from the SEDs of galaxies at $4.00 < z < 4.99$ and the IRAC channel 2 band from the SEDs of galaxies at $5.06 < z < 5.31$. This correction removes potential SED contamination by the Hα and [O III]λ5007 rest-optical lines. As in D18, we performed the SED fits using a combination of a fixed metallicity of 1.4 times the solar metallicity ($Z = 0.02$) and a Calzetti extinction curve (Calzetti et al. 2000), or else a fixed metallicity of 0.28 $Z_\odot$ and an SMC extinction curve (Gordon et al. 2003). This method of SED fitting was initially described in Reddy et al. (2018). The star formation history was set at either constant or exponentially increasing. The fits were performed with ages > 10 Myr allowed, and then with only those >50 Myr. With these different assumptions, we fit for stellar mass (M_*), ages younger than the age of the Universe, star formation rate (SFR), and $E(B-V)$ from 0.00 to 0.60. Given that the quality of the fits of each model was similar, we adopted the best-fitting parameters of 0.28 $Z_\odot$, SMC attenuation, constant star formation history, and age >50 Myr models. This choice was motivated by the fact that a sub-solar metallicity with an SMC extinction curve has been demonstrated to fit the IRX-β relationship better than other models at $z >$ (Oesch et al. 2013; Bouwens et al. 2016). Ages were constrained to >50 Myr so as to not be shorter than the typical dynamical time-scales of distant star-forming galaxies (assuming a relaxed disc and ignoring

[2]Available at https://irsa.ipac.caltech.edu/data/COSMOS/datasets.html

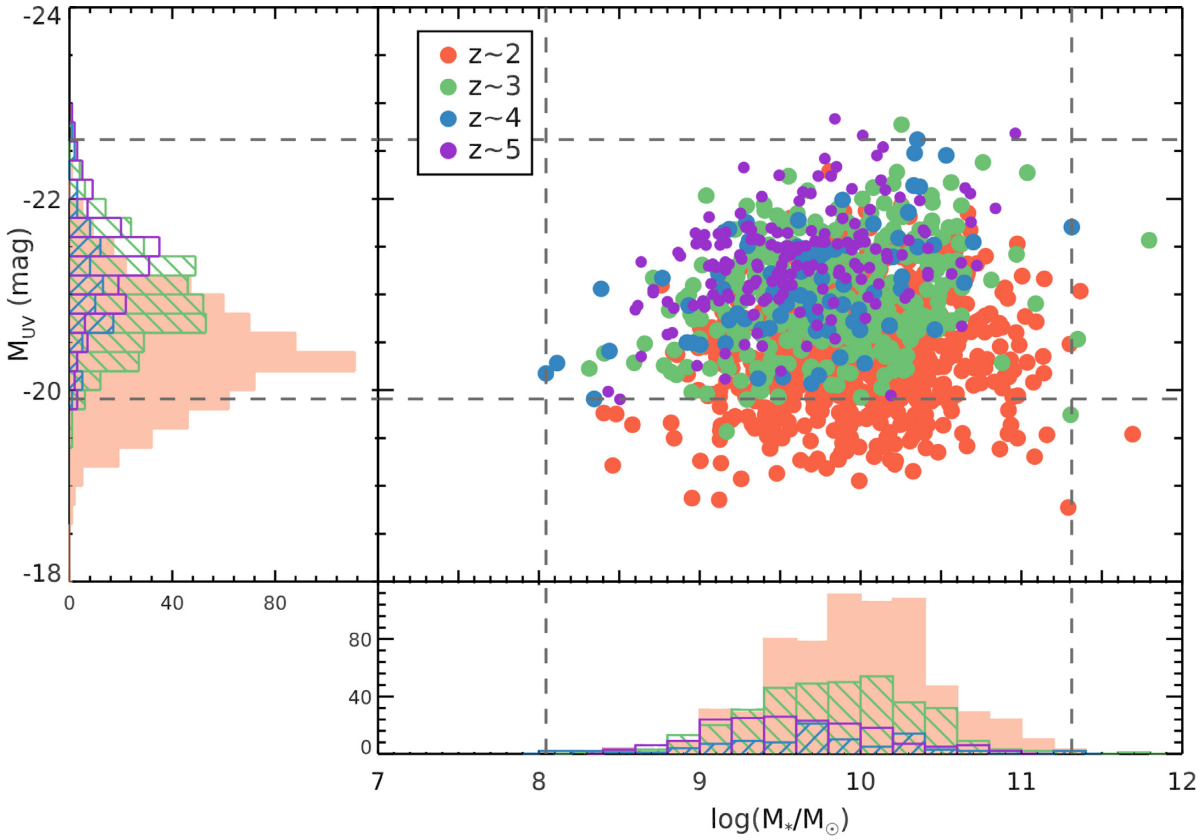

Figure 5. Absolute UV magnitude ($M_{\rm UV}$) versus stellar mass (M_*) for the four redshift samples. The distributions of $M_{\rm UV}$ and M_* are displayed in the histograms to the left and below the scatterplot. The cuts performed on the $z \sim 2$–4 data are shown as vertical and horizontal dashed lines.

Table 1. Median properties of the controlled $z \sim 2$–5 samples.

	$z_{\rm med}$	$M_{\rm UV}$	$\log(M_*/{\rm M}_\odot)$	$E(B-V)$	Sample size
$z \sim 2$	2.267	−20.51	10.00	0.09	539
$z \sim 3$	2.925	−21.00	9.87	0.08	309
$z \sim 4$	3.856	−21.06	9.72	0.04	91
$z \sim 5$	4.521	−21.33	9.80	0.05	175

the time-scales of local gas motions, Reddy et al. 2012), and a constant SFR was assumed for consistency with past work (Reddy et al. 2012; Steidel et al. 2014; Strom et al. 2017; Du et al. 2018). The SED fitting of the $z \sim 4$ sample in D18 was performed in a similar way. For the $z \sim 2$–3 galaxies, the 1.4 $Z_\odot$ + Calzetti model was used as they produced overall lower χ^2.

In order to perform a controlled study across redshift of galaxies with comparable properties, we restricted the $z \sim 2$, 3, 4, and 5 samples to span the same range in stellar mass and rest-UV luminosity. We examined the distribution of M_* determined by the SED fits and the UV absolute magnitude ($M_{\rm UV}$) in Fig. 5. The M_*–$M_{\rm UV}$ cuts performed in D18 of ($-22.62 < M_{\rm UV} < -19.91$) and [$8.04 < \log(M_*/{\rm M}_\odot) < 11.31$] are displayed as vertical and horizontal lines in the figure. These cuts remove low-luminosity objects in the $z \sim 2$ sample. The M_* and $M_{\rm UV}$ of the $z \sim 5$ sample span much of the same range as the $z \sim 4$ sample. Since the $z \sim$ 2–3 samples were already truncated to match the $z \sim 4$ sample, we perform no stricter M_*–$M_{\rm UV}$ cut on the $z \sim 2$ and $z \sim 3$ samples. The median $M_{\rm UV}$ and M_* of each sample within the D18 cuts are recorded in Table 1, along with other median sample properties from the SED fitting. The similarity of the $M_{\rm UV}$ and M_* medians further motivates that no additional cut is needed. After applying the D18 limits in M_* and $M_{\rm UV}$, we find the number of objects in the $z \sim 2$, 3, 4, and 5 samples are 539, 309, 91, and 175, respectively.

3 METHODS

Our goal is to examine the properties of the rest-UV spectral features of our different samples, including Ly α; LIS lines of Si II λ1260, O I λ1302 +Si II λ1304, C II λ1334, and Si II λ1527; and HIS lines of Si IV $\lambda\lambda$1393, 1402 and C IV λ1548, 1550. While Ly α can be well detected at $z \sim 5$ due to its large typical EW, it is difficult to detect the full suite of LIS and HIS lines in individual spectra, given their typical EWs of $\sim$ 1–2 Å. Thus, we rely on stacks of spectra in bins of various galaxy properties to reveal the characteristic strengths of the LIS and HIS lines. The Ly α line is known to have an important role in a galaxy's spectrum, strongly correlating with rest-UV spectral morphology (Shapley et al. 2003), motivating its choice as a sorting parameter and the creation of composites in bins of Ly α EW. Ly α EW, as opposed to Ly α luminosity, is normalized to the UV continuum and probes the efficiency of Ly α photon production and escape. The methods in this section broadly follow those described in D18. In addition, we consider here for the first time the increasing degree of IGM attenuation on average as a function of increasing redshift, quantifying this effect using the models of Laursen, Sommer-Larsen & Razoumov (2011).

3.1 Ly α equivalent width in individual spectra

In order to construct composite spectra spanning a range of Ly α EWs, we required an individual measurement of Ly α for each

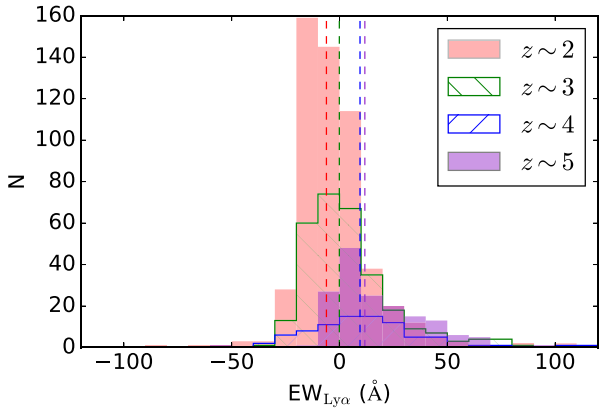

Figure 6. Rest-frame EW$_{Ly\,\alpha}$ distribution as a function of redshift. The $z \sim 2$, 3, and 4 samples are from D18. The median EW$_{Ly\,\alpha}$ for each sample is displayed as a vertical, dashed line. These medians increase towards stronger emission with increasing redshift.

object. We used the fitting method of Kornei et al. (2010) to measure Ly α EW. First, the rest-frame spectra were examined individually to determine whether the spectrum at 1216 Å follows an 'emission', 'absorption', 'combination', or 'noise' profile. The large majority of our sample were fit using 'emission' or 'noise', representing either a positively peaked, visible feature or no discernible one, with only one object following an 'absorption' profile consisting of a trough at 1216 Å and four objects following a 'combination' profile of a blueside trough and redside peak.

The continuum level was then determined using the following procedure: the redside continuum was calculated as the average of the flux values of the spectrum between 1225 and 1255 Å. If the spectrum had coverage blueward of 1120 Å, the blueside continuum was estimated as the average of the flux between 1120 and 1180 Å. If the spectrum only had coverage down to 1160 Å, the blueside continuum was averaged between 1160 and 1180 Å. If the spectrum did not have coverage to 1160 Å, the blueside continuum value was estimated by multiplying the redside value by the mean ratio of blue-to-red of 0.260, as determined from the remaining 140 objects of the sample with blueside coverage. The blueside continuum is suppressed relative to the redside due to absorption by the IGM. For 14 of the objects, the redside continuum was not well detected, leading to a ∼zero continuum value well within the 1σ noise of the spectrum. In order to measure an EW for these galaxies, we estimated the continuum flux photometrically. This estimate was obtained using the best-fitting SED of the object as described in Section 2.5, averaging in the same wavelength window of 1225–1255 Å. These 14 spectra were also normalized over the wavelength interval 1300–1500 Å so the continuum estimated from the spectra matched those from the photometry. For the objects with a well-detected continuum, this photometric estimation was also performed and compared to the spectroscopically determined values to ensure consistency between the measurements.

For spectra classified as 'emission', 'combination', or 'absorption', the Ly α flux was integrated between the wavelengths at which the full Ly α profile intersected the blueside and redside continuum values. For 'noise', the spectrum was integrated over a fixed window of 1210–1220 Å. Finally, the EW was measured as the ratio of the integrated Ly α flux and the redside-continuum flux density. The Ly α EW distribution of the four redshift samples is shown in Fig. 6. The median Ly α EW of each sample is overplotted on the corresponding histogram as a vertical line, indicating the evolution of the strength of Ly α within our four samples of increasing redshift. The sample median Ly α EWs are −6.07, −0.08, 9.51, and 11.75 Å for redshifts 2, 3, 4, and 5, respectively. This evolution must be interpreted in the context of the incompleteness of our $z \sim 5$ sample. We find that 38.6 per cent of objects at $z \sim 5$ had a systemic redshift measurement based only $z_{Ly\,\alpha}$, compared to 56.3 per cent at $z \sim 4$. In past work, a weak evolution of Ly α emitting fraction has been found at these redshifts (Stark et al. 2010). We do not find a significant tail in the EW$_{Ly\,\alpha}$ distribution at values less than 0 Å (i.e. absorption) at $z \sim 5$. However, we argue that, as the $z \sim 5$ sample is not significantly biased in redshift measurement method or colour–colour space (Fig. 3), it is also not significantly biased with respect to the underlying Ly α EW distribution – at least compared with $z \sim 4$. See D18 for a discussion of sample completeness from $z \sim 2$ to $z \sim 4$.

3.2 Composite spectra

We first created composite spectra of the spectra in each redshift sample, and then split the samples into bins of various properties and generated composites of the spectra of the objects in each bin.

We generated composite spectra by performing a bootstrapping analysis of the objects in each sample. Based on the number of objects in the sample, we drew the same number of spectra from the bin with replacement. For each draw, we took each individual galaxy spectrum and normalized it to its photometric flux density. We then shifted it into the rest frame in L_λ units based on its measured systemic redshift. The rest-frame, L_λ spectrum of each object was then perturbed according to a Gaussian distribution with a standard deviation corresponding to the value of the error spectrum at that wavelength. These spectra were combined with the IRAF tool *scombine* using the combination mode 'average', with rejection of the three highest and three lowest flux values at each wavelength increment. This bootstrapping was performed 100 times, generating 100 composites, each representing a different sampling of spectra in the bin and reflecting the statistical noise in each individual spectrum. The resulting 100 spectra were then combined into a final science composite and error spectrum by taking the average L_λ and standard deviation at each wavelength increment.

We can examine the overall spectral characteristics of each sample with this composite method. The four composites of increasing redshift are presented in Fig. 7. The most striking difference in the $z \sim 5$ spectrum is the strength of its Ly α feature, reflecting the difference in median Ly α EW of the sample. The properties of the absorption features are difficult to distinguish qualitatively and require further analysis.

We split our redshift sample into bins of various properties. In addition to Ly α, these properties include $E(B-V)$ and integrated galaxy properties such as M_*, SFR, age, and M_{UV}. Depending on the property being examined, the set of objects comprising each bin change based on the spectral coverage of the objects. For examining LIS strength as a function of Ly α EW, we required every object in the sample to have coverage out to the most redward LIS line, Si II λ1527. This requirement slightly reduced our sample to 160 objects. We split this sample into four bins of increasing Ly α EW with 40 objects per bin. Using an equal number of objects per bin provides a comparable S/N for each composite spectrum. To examine HIS strength as a function of Ly α EW, we required coverage of the most redward HIS line, C IV λ1548, 1550. We divided the resulting sample of 154 objects into four bins of

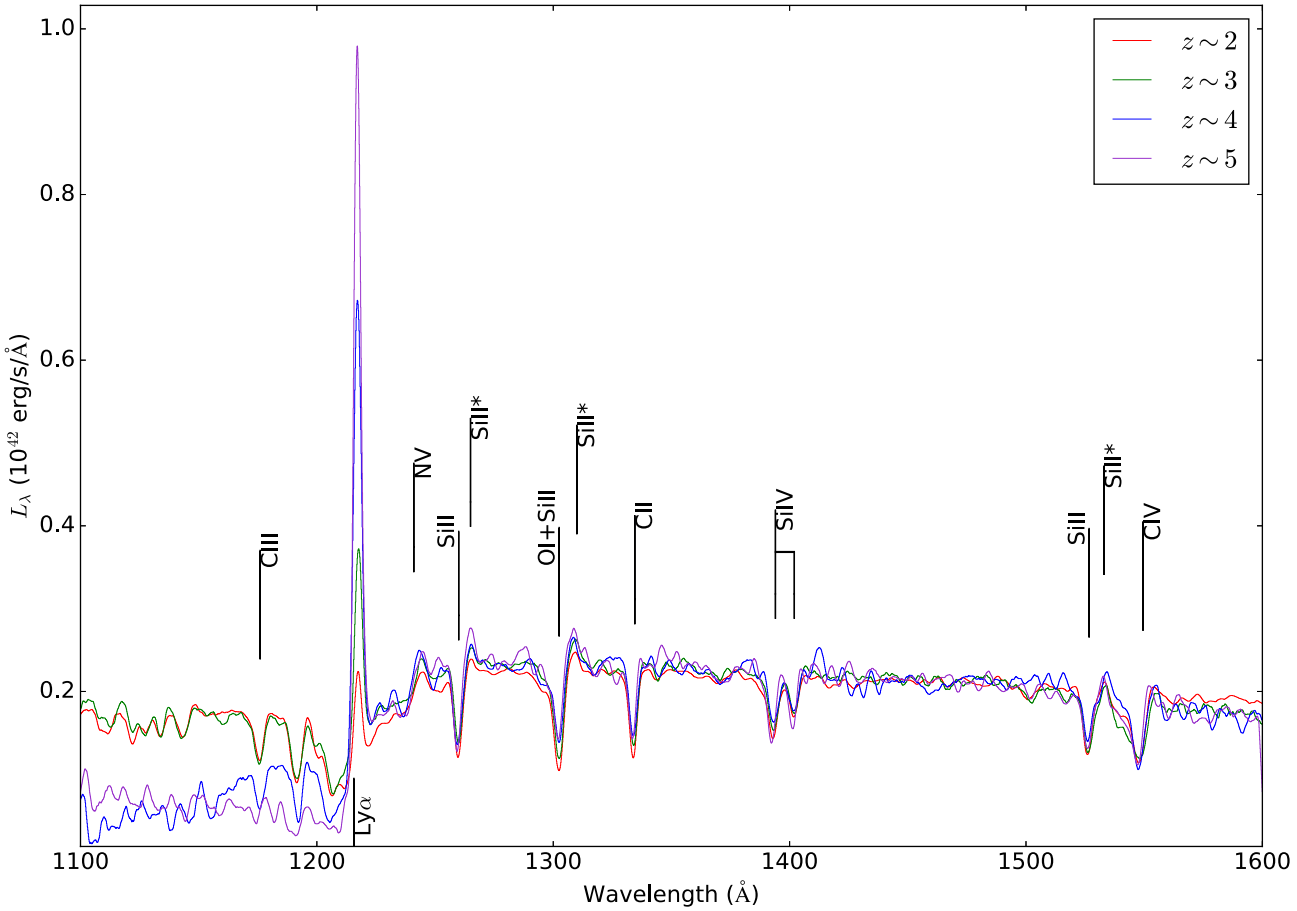

Figure 7. Composite spectra of the four redshift samples. These spectra were smoothed with a boxcar window of 3 Å. The $z \sim 2$–4 spectra were normalized to the $z \sim 5$ spectra using their respective median flux value in the range 1450–1500 Å. The rest-frame positions of various absorption and emission features are displayed.

increasing Ly α. Finally, we examined Ly α and LIS strength as a function of integrated galaxy properties using four bins of the 160 objects with coverage of Si II λ1527.

The four composite spectra binned by Ly α EW are shown in Fig. 8. The absorption features are clearly resolved in the composite spectra, and the variation of the Ly α EW in each bin can be seen in the profile at 1216 Å. From these composites, we can remeasure the Ly α EW and measure the EW of interstellar absorption features. To determine the Ly α EW of each bin, we applied the fitting technique described in Section 3.1 to each of the bootstrapped spectra, representing the variation in each composite bin of Fig. 8. The final Ly α EW and 1σ error reported for each bin was the mean and standard deviation of these 100 measurements. This measured Ly α EW from stacked spectra and the median Ly α EW of the objects composing each bin were comparable within 1σ.

To understand how our analysis is affected by the changing intrinsic brightness of the galaxies, we examined the $M_{\rm UV}$ of each galaxy as a function of its measured Ly α EW. All the galaxies in our $z \sim 5$ sample are plotted in $M_{\rm UV}$–EW$_{\rm Ly\,\alpha}$ space in Fig. 9. As Ly α emission strength increases, the galaxies tend to be dimmer in the UV continuum. The objects are split into four bins of increasing Ly α EW, and the median $M_{\rm UV}$ and Ly α EW are displayed. The median $M_{\rm UV}$ of the lowest EW$_{\rm Ly\,\alpha}$ bin is -21.44, while the highest bin has a median $M_{\rm UV}$ of -21.11. While we observe a trend of fainter $M_{\rm UV}$ with increasing EW$_{\rm Ly\,\alpha}$, just as that found within the $z \sim$ 3–4 samples of D18, this dependence is weak. Accordingly, it is reasonable to interpret differences in EW$_{\rm Ly\,\alpha}$ as being dominated by variations in emergent Ly α flux.

3.3 IGM correction to Ly α equivalent widths

In order to obtain a more accurate measurement of the intrinsic Ly α production and escape through the ISM, we attempted to remove the effects of IGM attenuation on the strength of the observed Ly α line. The IGM transmission in the vicinity of the Lya feature decreases noticeably from $z \sim 2$ to $z \sim 5$. To quantify this evolution, Laursen et al. (2011) generated sightlines through high-resolution cosmological simulations of galaxy formation, where the simulated sightlines originate in samples of galaxies at different redshifts ranging from $z = 2.5$ to 6.5. These authors produced the mean IGM transmission profile in the vicinity of Ly α at each redshift, showing how its shape and depth evolve towards stronger absorption at higher redshift. We interpolated the model of Laursen et al. (2011) to produce IGM transmission curves appropriate for the median redshift of each of our four redshift samples.[3]

[3]We note that each IGM transmission curve has an associated uncertainty based on the range of sightline opacities found in the simulations of (Laursen et al. 2011). Given that this uncertainty for the average of ∼40 sightlines is subdominate compared to our other uncertainties, we did not take it into account.

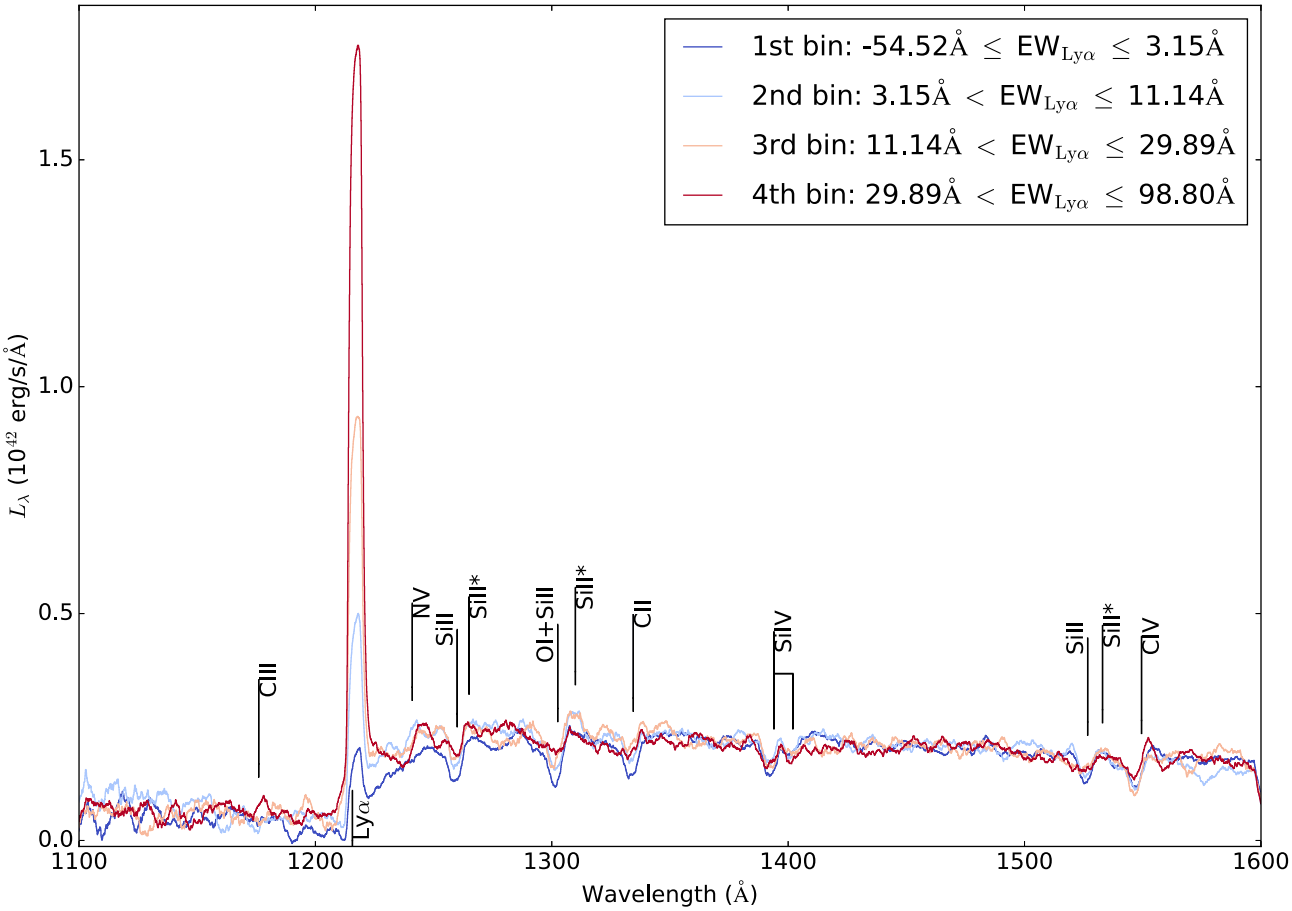

Figure 8. Composite spectra of the $z \sim 5$ sample in bins of increasing Ly α EW. The dark blue spectrum corresponds to the objects with the lowest EW$_{Ly\alpha}$, while the dark red contains the objects with the highest EW$_{Ly\alpha}$. Each composite spectrum is constructed from the spectra of 34 objects characterized by the EW$_{Ly\alpha}$ ranges displayed in the legend. The variation of rest-UV spectral features as a function of increasing EW$_{Ly\alpha}$ can be qualitatively observed near the wavelengths of various LIS and HIS lines labelled by solid black lines.

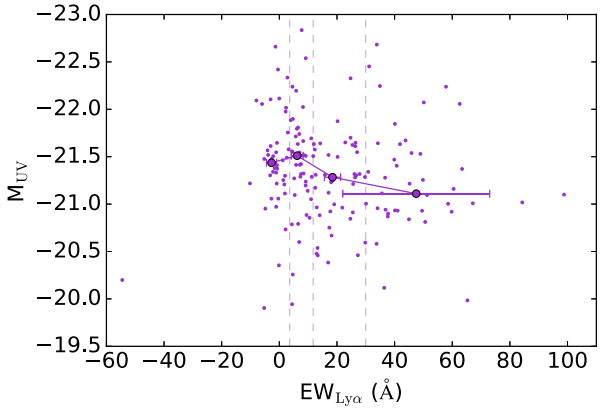

Figure 9. Absolute UV magnitude (M_{UV}) versus EW$_{Ly\alpha}$. Individual detections are displayed as smaller circles. The sample is divided into bins of increasing Ly α EW, with these divisions shown as vertical, dashed lines. The median properties of the objects of each bin are plotted as larger, filled circles.

We then degraded the curves in a manner that represented the process of observing our galaxy spectra at moderate resolution and combining them with uncertain systemic redshifts into composite spectra. Specifically, we smoothed the model IGM transmission curve by a Gaussian kernel to match the average spectral resolution of each composite: $R_{average} \sim 970$, 1280, and 2700 for the $z \sim 2$–3, $z \sim 4$, and $z \sim 5$ samples, respectively. The more important blurring effect arises from the fact that the estimates of systemic redshift from Ly α and LIS features have associated systematic errors (i.e. they are based on mean relations between Ly α or LIS redshifts and systemic redshifts, which have intrinsic scatter). In order to simulate the effect of stacking N spectra with uncertain systemic redshifts, we generated N individual IGM transmission curves and perturbed each curve by a small $\Delta\lambda$. The value $\Delta\lambda$ was drawn from a normal distribution with zero mean and a standard deviation of $\sigma_{\Delta\lambda} = (\sigma_z/(1+z)) \times 1215.67$ Å. The redshift uncertainty σ_z was calculated through the method described in Section 2.2. The resulting N perturbed (in wavelength) transmission curves were then averaged together. The transmission curves calculated in this way for the $z \sim 2$–5 samples are shown in the bottom panel of Fig. 10. The fraction of photons transmitted by the IGM at 1215.67 Å decreases substantially towards $z \sim 5$.

In order to convert the transmitted Ly α profiles to those intrinsic to the galaxy, we divided the observed composite spectra by the associated degraded IGM transmission curve. Both the transmitted and intrinsic Ly α profiles of the $z \sim 2$–5 samples are shown in the top panel of Fig. 10. The Ly α profiles in composite spectra at higher redshift receive larger positive corrections for IGM absorption. This analysis was applied to the composites of the

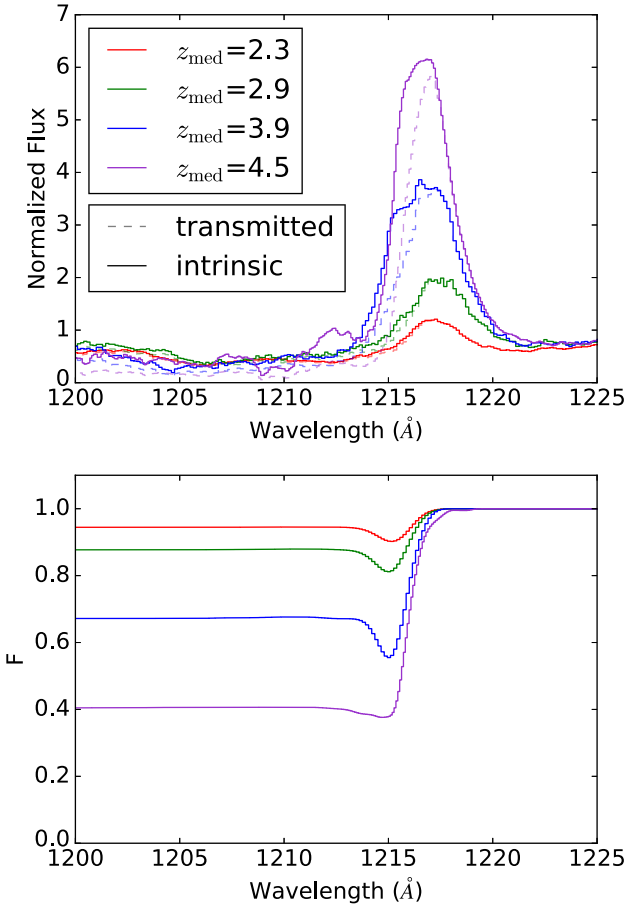

Figure 10. IGM correction method applied to the $z \sim 2$–5 composites spectra. *Top panel:* Ly α profiles for $z \sim 2$–5 sample composites, with and without IGM attenuation correction applied. The observed composites transmitted through the IGM are displayed as dashed lines, and the intrinsic Ly α profiles are displayed as solid lines. The intrinsic profiles were determined by dividing the transmitted profiles by the transmission curves shown in the bottom panel. *Bottom panel:* Degraded IGM transmission curves calculated at $z = 2.3$, 2.9, 3.9, and 4.5. Transmission curves were calculated at a given redshift by interpolating the models of Laursen et al. (2011) and were degraded based on the average spectral resolution of each redshift sample and the systemic redshifts of the objects contained in each sample.

$z \sim 2-5$ samples binned by Ly α EW and galaxy properties, and the Ly α EW of each composite was remeasured as described in Section 3.2.

3.4 Absorption line equivalent width

For each composite spectrum, we measured both LIS and HIS EWs. First, we normalized the continua of the rest-frame, L_λ spectra using the IRAF tool *continuum*, using a fourth-order spline fit with continuum regions that avoid the spectral features defined by Rix et al. (2004). From the normalized spectra, we then fit each absorption feature with a Gaussian profile using the scipy routine *leastsq*, with initial fit parameters corresponding to the rest-frame central wavelength of the line and a linewidth of $\sigma = 2$ Å, typical of composite LIS lines at $z \sim 5$. To calculate the flux of each line, we integrated the composite spectrum about the central wavelength of the Gaussian fit to the line using an integration window that spanned from $-3\sigma_v$ to $+3\sigma_v$. Here, σ_v is defined as the standard deviation in velocity space of the average of the four key LIS profiles under consideration. In order to determine σ_v, we converted the four LIS profiles from rest-frame wavelength space to velocity space and averaged them at each velocity increment. We then fit a Gaussian function to the combined absorption profile in velocity space using the scipy routine *leastsq*, leading to an estimate of σ_v. This technique yielded an integration window for each LIS feature that was informed by the average width of the LIS lines in the composite spectrum. At the same time, averaging the four LIS features in velocity space mitigated the effects of low-quality individual profile fits. We finally calculated the EW of the absorption feature by dividing this flux by the normalized continuum value in the integration window. The error on the EW measurement was determined via propagation of errors from the error spectrum in the integration window. The continuum-normalized spectra in bins of increasing Ly α EW are shown in Fig. 11. The fits to the Gaussian profiles of the LIS lines of Si II λ1260, O I λ1302 +Si II λ1304, C II λ1334, and Si II λ1527 are displayed in detail here. The integration windows of ±5 Å are also displayed, with the entirety of the line profiles fitting in these windows.

For the HIS doublet of Si IV λλ1393, 1402, a double Gaussian profile was fit to the line in the same method described for the single profiles, above. Additionally, the central-wavelength ratio of the doublet members was fixed at the theoretical value of (1402.770/1393.755). The integration window was set to range from −5 Å of the centre of the bluer profile up to +5 Å of the centre of the redder profile. These Si IV λλ1393, 1402 fits in four bins of increasing $\rm EW_{Ly\alpha}$ are shown in the left-hand panels of Fig. 12.

The C IV λ1548, 1550 profile is more complex: on top of the blended absorption feature, there is a stellar component produced by high-velocity winds in O and B stars (Du et al. 2016, and references therein). This stellar component must be removed before the absorption from the interstellar gas can be measured. While a stellar P-Cygni component can appear on the Si IV λλ1393, 1402 absorption feature, the component is less significant within the mass ranges and corresponding metallicity ranges of our samples (Steidel et al. 2014; Sanders et al. 2018), thus does not require modelling and removal. We used the rest-frame UV model starburst spectra of Leitherer et al. (2010), smoothed to the resolution of our data, to represent the stellar component. We fit the templates, evaluated at 0.05 $Z_\odot$, 0.2 $Z_\odot$, 0.4 $Z_\odot$, $Z_\odot$, and 2 $Z_\odot$, and combined the two bracketing (or one adjacent for the lowest and highest metallicities) best-fitting models. This fit is performed on the blue wing of C IV λ1548, 1550 between 1535 and 1544 Å, and we refer readers to fig. 3 of Du et al. (2016) for an illustration of our fitting method. By dividing the continuum-normalized spectra by the best-fitting stellar template, we effectively removed the stellar component of C IV λ1548, 1550. We then measured the EW of the interstellar component of C IV λ1548, 1550 using the method previously described for the single LIS lines, as the doublet is blended together into a single profile at our spectral resolution. The fits to the C IV λ1548, 1550 interstellar profile after removing the stellar component are shown in the right-hand panels of Fig. 12.

4 RESULTS

In this section, we examine the properties of our $z \sim 5$ sample as a function of binned properties of Ly α EW, $E(B-V)$, stellar mass, $M_{\rm UV}$, age, and SFR.

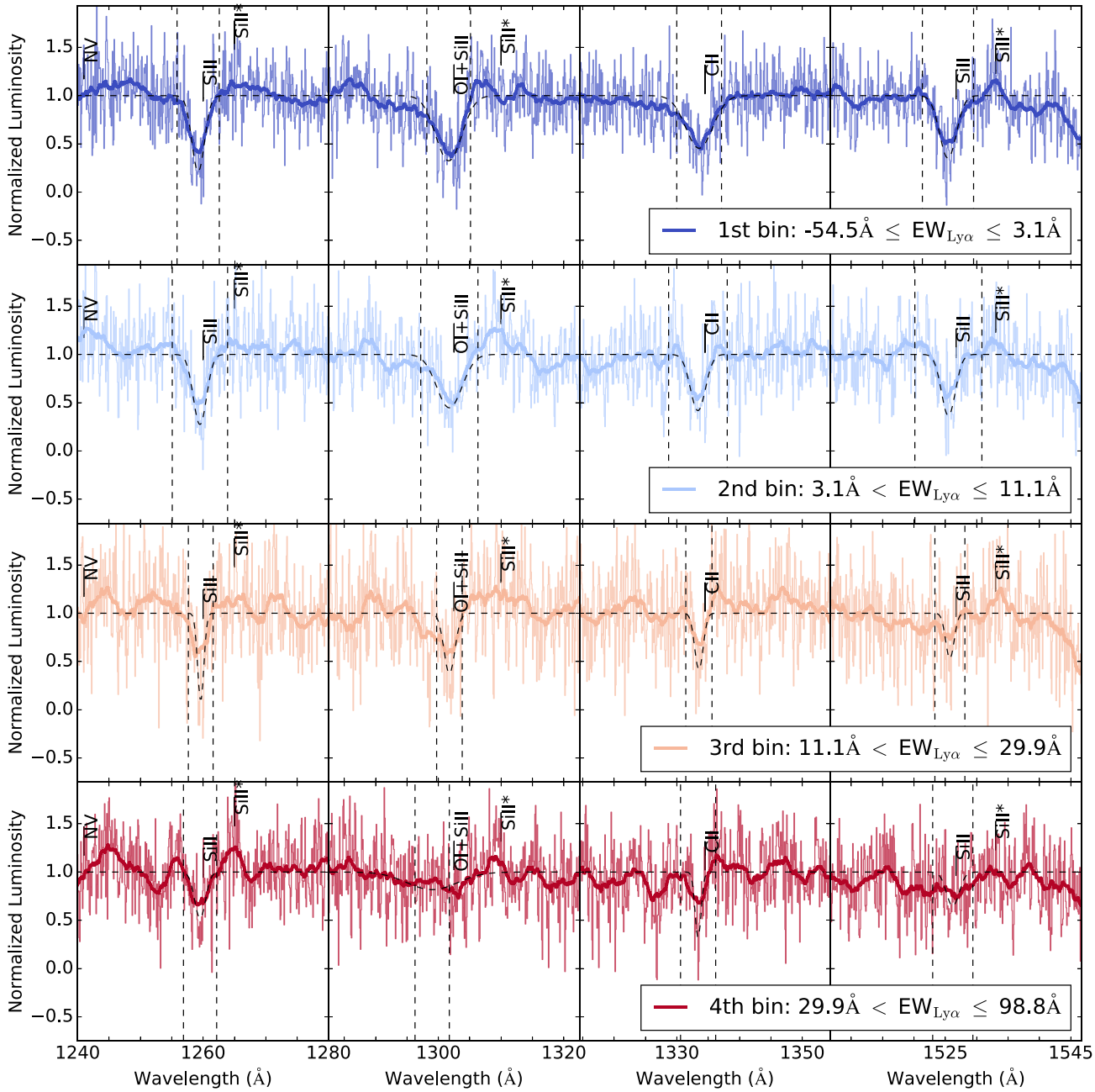

Figure 11. Fits to the four LIS features of the composite spectra of the $z \sim 5$ sample, split into four bins with EW$_{Ly\alpha}$ decreasing from the top to the bottom row. These EW$_{Ly\alpha}$ bins are the same as those shown in Fig. 8. The more transparent spectra in each row are the continuum-normalized, rest-frame, L_λ spectra from which measurements were performed. The more opaque spectra are convolved with a boxcar window of width 3 Å for easier viewing. The vertical, dashed lines illustrate the ±5 Å integration windows from which EW measurements were made.

4.1 Line strength

We are motivated by a physical picture in which the strength of LIS absorption probes the covering fraction of neutral gas in a galaxy (Reddy et al. 2016). Thus, with the reasonable assumption of a roughly spherically symmetric gas distribution (e.g. Law et al. 2012), there will be a connection between the Ly α photons, which are scattered by any neutral gas covering the galaxy (Steidel et al. 2010), and the resulting strength of the LIS absorption features. In contrast, there is evidence that the HIS lines exist in an ionized medium, physically distinct from the neutral gas (Shapley et al. 2003; Du et al. 2016, 2018). HIS features have been found to have similar kinematics as LIS lines (Pettini et al. 2002; Heckman et al. 2015; Chisholm et al. 2016; Berg et al. 2018), however Du et al. (2016) finds that while the kinematics of HIS and LIS lines are similar, they correlate differently with galaxy properties, indicating they may exist in different ISM phases. A lack of relationship between Ly α and HIS will support this picture.

To quantify the strength of the LIS lines, we measure EW$_{LIS}$ as the weighted average of the Si II λ1260, O I λ1302 + Si II λ1304, C II λ1334, and Si II λ1527 EWs and their associated errors. EW$_{LIS}$ is presented in the top left panel of Fig. 13 as a function of increasing EW$_{Ly\alpha}$. Here, the relationship between Ly α and EW$_{LIS}$ is presented

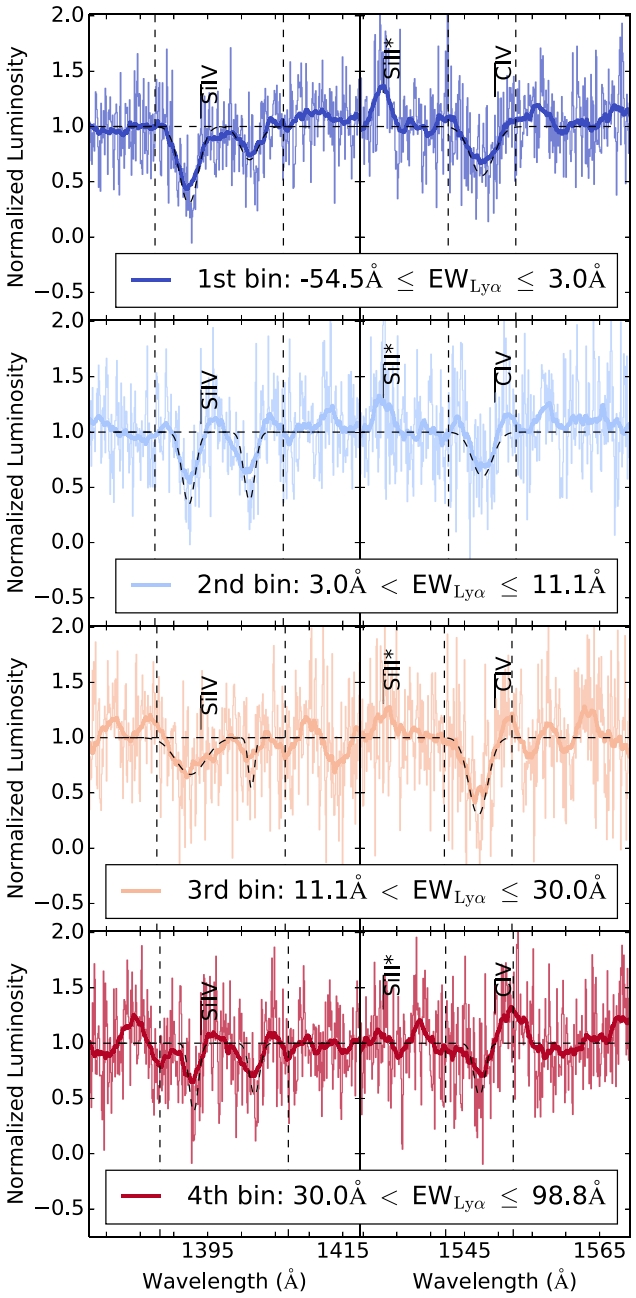

Figure 12. Fits to the Si IV$\lambda\lambda$1393, 1402 and C IV λ1548, 1550 features of the composite spectra of the $z \sim 5$ sample, split into four bins of increasing EW$_{Ly\alpha}$. These spectra have the stellar component of C IV λ1548, 1550 removed. The top panel corresponds to the objects with the lowest EW$_{Ly\alpha}$, while the bottom panel contains the objects with the highest EW$_{Ly\alpha}$. As in Fig. 11, the transparent spectra are the continuum-normalized, rest-frame, L_λ spectra from which measurements were performed. The opaque spectra are convolved with a boxcar window of width 3 Å for easier viewing. The vertical, dashed lines illustrate the ±5 Å integration windows from which EW measurements were made.

at $z \sim 5$ using the sample from this work, while the $z \sim 2$–4 data points are taken from D18. The Ly α EWs uncorrected for IGM absorption are connected by dotted lines, while the intrinsic Ly α EWs calculated by the method described in Section 3.3 are connected by solid lines. It can be seen that at $z \sim 5$ the Ly α EW range skews significantly higher than that at lower z, with the lowest EW bin at -1.8 ± 1.4 Å. The trends at lower redshift are largely unchanged at $z \sim 5$. This result implies that the attenuation of Ly α photons (i.e. due to scattering and dust absorption) and the strength of the LIS feature is intrinsically linked, and is fundamental across redshift. In the highest bin of EW$_{Ly\alpha}$, EW$_{Ly\alpha}$ is greater at fixed EW$_{LIS}$ compared to lower redshift, though within 1σ. This deviation suggests intrinsically stronger Ly α at fixed ISM covering fraction (but see e.g. McKinney et al. 2019). We further explore this result in Section 5.

As seen in Fig. 11, the shape of the LIS profiles is not strongly dependent on Ly α strength. The ratio of EW$_{Si\,II\lambda1260}$ / EW$_{Si\,II\lambda1527}$ can reflect the changing properties of the gas producing Si II absorption: when the ratio approaches ∼5, the ratio of their oscillator strengths, Si II is in the optically thin regime. The ratio of EW$_{Si\,II\lambda1260}$ / EW$_{Si\,II\lambda1527}$ in all EW$_{Ly\alpha}$ bins is roughly unity, indicating that these Si II features are in the optically thick regime. This result is consistent with Si II line ratios in the $z \sim 2$–4 samples presented in D18.

We also examine the evolution of the average spectral properties of the composites after the IGM correction was applied, shown as stars in the top left panel of Fig. 13. We see the overall composites following a similar linear relationship at $z \sim 2$–4, with the average Ly α emission strength increasing and LIS absorption strength decreasing with increasing redshift. We see an evolution off this linear relationship at $z \sim 5$, with the overall composite having stronger Ly α emission and similar LIS absorption properties as the $z \sim 4$ sample. We will further examine the average and binned spectral properties in a $z \sim 5$ subsample with higher median redshift in Section 5.

The EW$_{HIS}$ is defined as the weighted average of EW$_{CIV\lambda1548,1550}$ and EW$_{SiIV\lambda\lambda1393,1402}$. We display the relationship between EW$_{HIS}$ in bins of Ly α line strength in the lower left panel of Fig. 13. In D18, no significant relationship between HIS and Ly α strength was found at $z \sim 2$–4. In the $z \sim 5$ sample, we find similar strengths of EW$_{HIS}$, showing no redshift evolution in the overall strengths of the features. We also find no trend of stronger EW$_{HIS}$ as a function of stronger EW$_{Ly\alpha}$ emission, similar to what is observed at lower redshift.

In the highest quartile of EW$_{Ly\alpha}$ emission strength, we find evidence for nebular C IV emission at $z \sim 5$. This detection is shown in the bottom panel of Fig. 12. We discuss this spectral feature and its implications for the inferred metallicity of the $z \sim 5$ sample in Section 5.3.

4.2 $E(B-V)$

Of all the galaxy properties measured by SED fitting, dust attenuation is most directly tied to the makeup of the ISM and CGM. As dust grains preferentially scatter bluer light, the amount of reddening reflects the amount of dust along the line of sight. The reddening of the SED of high-redshift sources by dust is typically measured in terms of the quantity $E(B-V)$. The relationship between Ly α and $E(B-V)$ has been well demonstrated: stronger Ly α emission in galaxies correlates with a bluer SED (Shapley et al. 2003; Pentericci et al. 2007; Vanzella et al. 2009; Kornei et al. 2010). The scattering of Ly α photons through neutral gas in the ISM implies greater path lengths to interact with the dust in the galaxy. Shapley et al. (2003) explored the possibility of dust existing in the same phase as the neutral gas itself, implying a direct correlation between the neutral-gas covering fraction and dust reddening for non-resonant radiation, although uncertainty exists between whether the dust lies in outflowing gas or H II regions.

We examine the strength of Ly α in bins of increasing $E(B-V)$ in top right panel of Fig. 13. Individual detections of $E(B-V)$

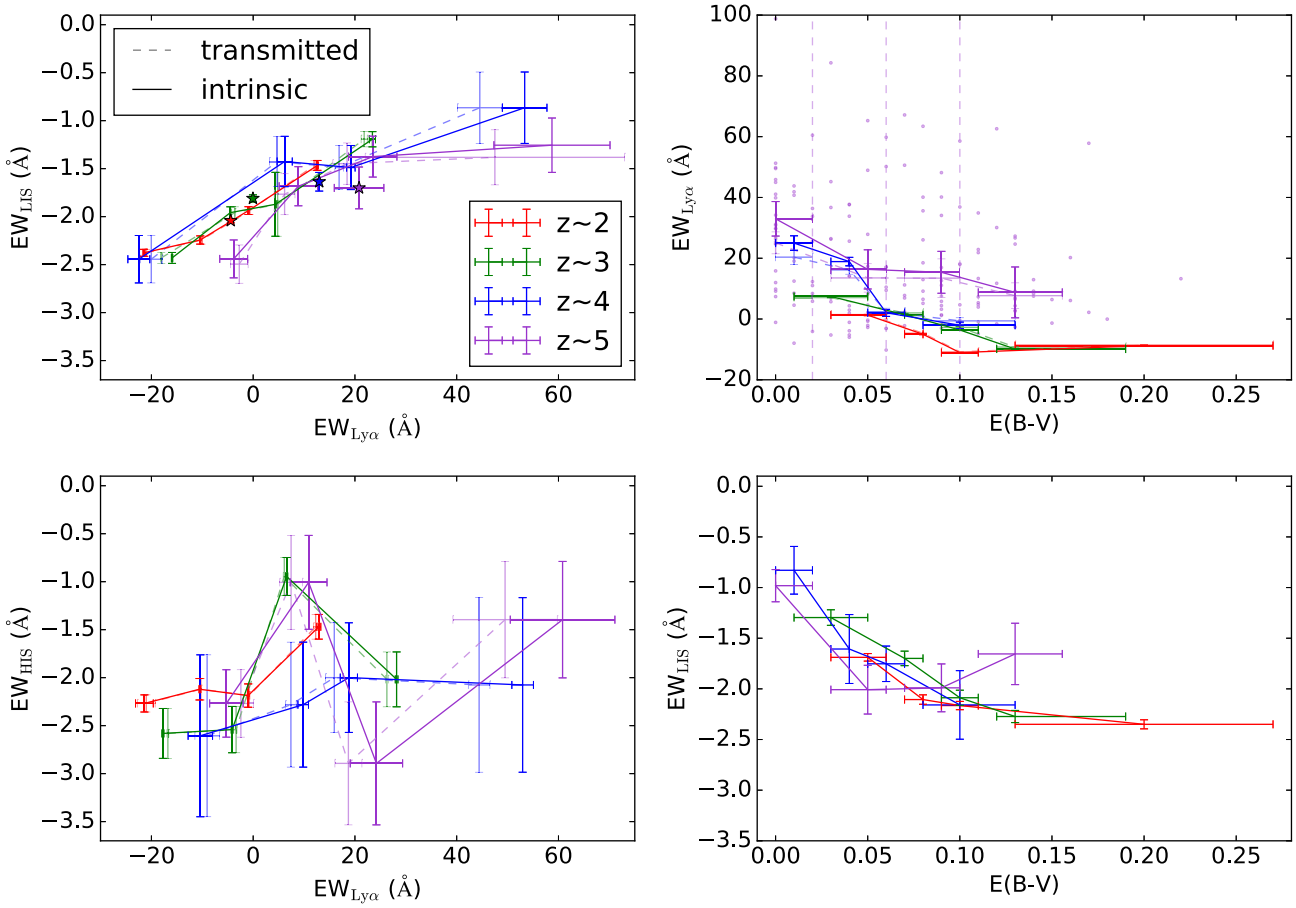

Figure 13. Relations between $EW_{Ly\alpha}$, EW_{LIS}, EW_{HIS}, and $E(B-V)$. $EW_{Ly\alpha}$, EW_{LIS}, and EW_{HIS} were measured from composite spectra. The measurements from the observed composites are displayed in transparent points connected by dotted lines, while the corrected measurements after application of degraded IGM transmission curves are the opaque points connected by solid lines. The purple points correspond to measurements of the $z \sim 5$ sample. The red, green, and blue points are of the $z \sim 2$, 3, and 4 samples of D18. *Top left panel:* EW_{LIS} versus $EW_{Ly\alpha}$. The redshift samples are divided into four bins of increasing $EW_{Ly\alpha}$, with $EW_{Ly\alpha}$ and EW_{LIS} measured from composite spectra composed of the objects in each bin. The average measurements of the $z \sim 2$–5 samples are displayed as stars. *Bottom left panel:* EW_{HIS} versus $EW_{Ly\alpha}$. The binned samples are the same as in the top left panel, with the exception that the objects were required to have coverage of C IV λ1548, 1550. EW_{HIS} and $EW_{Ly\alpha}$ are also measured from composite spectra, made from combining the individual spectra of the objects in each $EW_{Ly\alpha}$ bin. *Top right panel:* $EW_{Ly\alpha}$ versus $E(B-V)$. The points are the redshift samples divided into four bins of increasing $E(B-V)$, with $EW_{Ly\alpha}$ measured from composite spectra and $E(B-V)$ from the median of the objects in each bin. The transparent points are individual detections of the $z \sim 5$ sample. *Bottom right panel:* EW_{LIS} versus $E(B-V)$. The binned samples are the same as the top right panel, with EW_{LIS} also measured from composite spectra.

and $EW_{Ly\alpha}$ are overplotted as transparent points. The trends shown by the solid purple line, corresponding to measurements post-IGM correction at $z \sim 5$, are consistent with the well-established inverse-correlation between $EW_{Ly\alpha}$ and $E(B-V)$ that pertains all the way down to $z \sim 0$ (Hayes et al. 2014). The $z \sim 2$–4 sample of D18 follows a similar decreasing trend, although the consistency breaks down at larger $E(B-V)$. Here, $EW_{Ly\alpha}$ is larger at fixed $E(B-V)$ in the $z \sim 5$ sample compared to lower redshift. We also calculate the correlation between the individual transmitted $EW_{Ly\alpha}$ and $E(B-V)$ measurements in our sample. We perform a Spearman correlation test, with a null hypothesis that $EW_{Ly\alpha}$ and $E(B-V)$ are uncorrelated in the $z \sim 5$ sample. The Spearman test produces a correlation coefficient of −0.27 with a p-value of 0.000 45, strongly rejecting the null hypothesis. This test further supports that the inverse correlation between $EW_{Ly\alpha}$ and $E(B-V)$ continues out to $z \sim 5$.

The strength of EW_{LIS} in bins of increasing $E(B-V)$ is presented in the lower right panel of Fig. 13. The $z \sim 5$ trend also follows the one at $z \sim 2$–4, with larger $E(B-V)$ leading to a stronger LIS detection. This result supports the physical picture of dust grains existing in the same phase of gas as that attenuating Ly α and strengthening the LIS absorption (Reddy et al. 2016). This trend also appears to be invariant out to $z \sim 5$. The question of which relation is most fundamental – LIS–$E(B-V)$ or LIS–Ly α – is difficult to surmise from these plots, but has important implications for the relationship between dust, neutral-phase gas, and escaping Ly α radiation from a galaxy. In Section 5, we re-examine the evolution of the relationships among Ly α, LIS, and $E(B-V)$ using finer redshift divisions at $z > 4$, and gain further insights into this important question.

4.3 Other galaxy properties

In addition to $E(B-V)$, we examine the strength of Ly α binned in terms of galaxy properties of M_*, SFR, age, and M_{UV}. These relationships out to $z \sim 5$ are presented in Fig. 14. Both the intrinsic and transmitted $EW_{Ly\alpha}$ are shown as solid and dashed

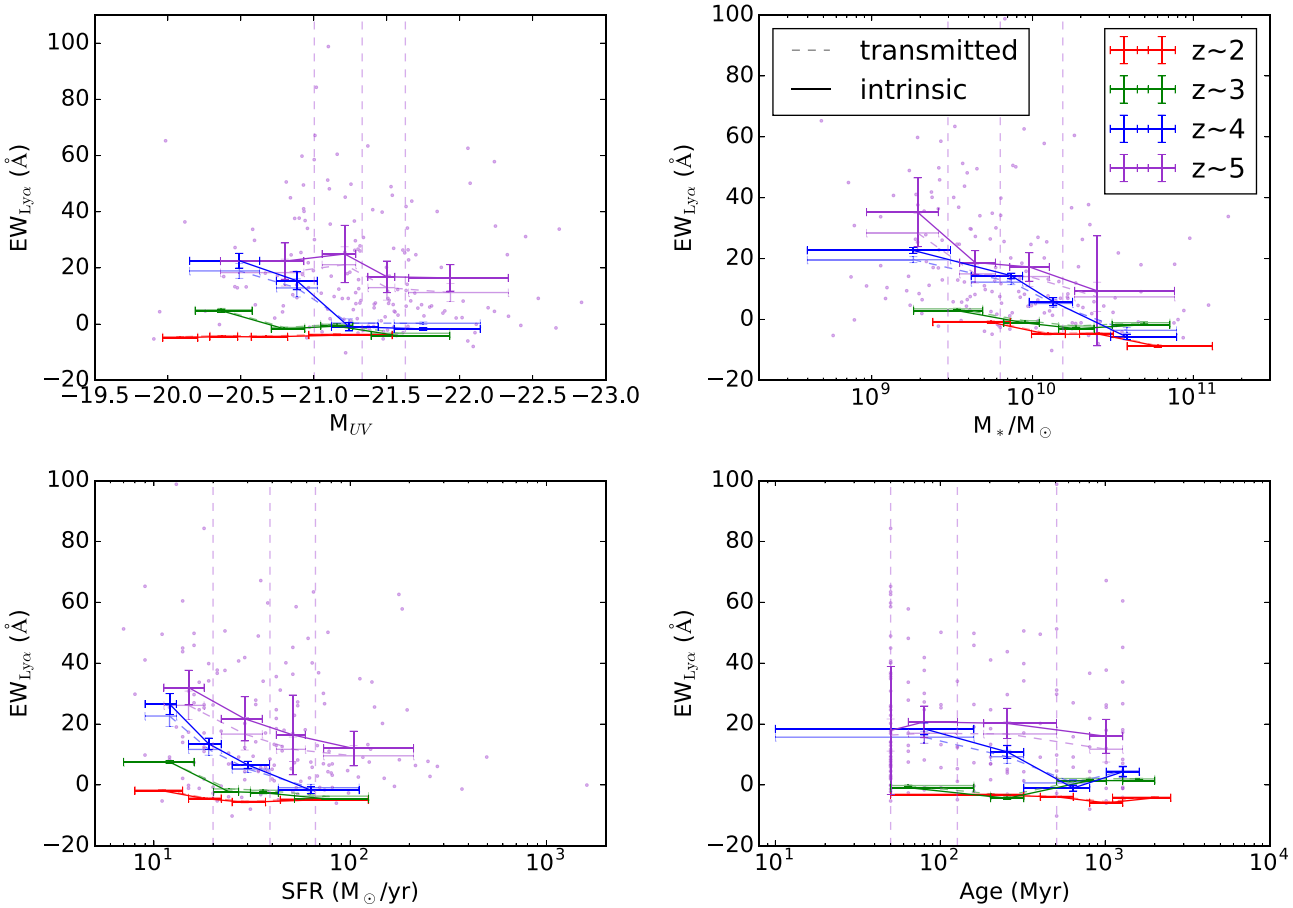

Figure 14. EW$_{Ly\alpha}$ as a function of integrated galaxy properties. Within each panel, each redshift sample is divided into four bins of an increasing galaxy property corresponding to that displayed on the *x*-axis: clockwise from top left, M_{UV}, M_*, age, and SFR. The dashed lines connect measurements of EW$_{Ly\alpha}$ from the composite spectra and the median galaxy property of the objects in each bin. The solid lines represent the same measurements after applying the IGM transmission curves of Laursen et al. (2011). The purple points are the individual measurements of EW$_{Ly\alpha}$ and galaxy property determined in this work for the $z \sim 5$ sample. The vertical, purple, dashed lines represent the borders of the bins of the respective galaxy property.

lines, respectively, and the individual transmitted measurements for each object are shown as purple points.

Most of these relationships extend those that are present at $z \sim 2$–4. At $z \sim 5$, we find that stronger EW$_{Ly\alpha}$ emission occurs in fainter galaxies, albeit weakly, similar to the trend observed at $z \sim 4$. This trend is skewed towards stronger EW$_{Ly\alpha}$ emission at fixed brightness at $z \sim 5$. The relationship between M_{UV} and EW$_{Ly\alpha}$ flattens in the lower redshift samples. We find a similar behaviour in SFR space, where we find greater EW$_{Ly\alpha}$ emission in galaxies with lower SFR, and greater EW$_{Ly\alpha}$ at fixed SFR at $z \sim 5$ compared to $z \sim 2$–4. In stellar-mass space, we find stronger EW$_{Ly\alpha}$ emission in less-massive galaxies, but the trend does not appear to evolve beyond that at $z \sim 4$. Massive galaxies tend to be more dusty (Garn & Best 2010; Whitaker et al. 2017; McLure et al. 2018), which would suppress their EW$_{Ly\alpha}$. We find no trend between EW$_{Ly\alpha}$ and age at $z \sim 5$, consistent with results at $z \sim 2$–4. This lack of trend could be explained by EW$_{Ly\alpha}$ reaching equilibrium quickly after the onset of a starburst (50–100 Myr, see Verhamme et al. 2008).

We also examine the correlation between $\Delta v_{Ly\alpha\text{–LIS}}$ and EW$_{Ly\alpha}$ and recover the anticorrelation of Shapley et al. (2003), indicating that a Lyα velocity peak closer to systemic indicates an easier pathway of escape for Lyα photons. This anticorrelation is weak, with a Spearman correlation test producing a correlation coefficient of -0.17 and a *p*-value of 0.14.

In summary, at $z \sim 5$, we find similar trends to those at $z \sim 4$: galaxies with stronger Lyα emission tend to have lower SFRs, less star formation, bluer UV continua, and less dust extinction. We also find stronger EW$_{Ly\alpha}$ emission at fixed galaxy property in the $z \sim 5$ sample.

5 DISCUSSION

Cosmic reionization is the phase change of neutral to ionized hydrogen in the IGM, which appears to be roughly finished by $z \sim 6$ (Fan et al. 2006; McGreer, Mesinger & D'Odorico 2015). The leading theory is that reionization was caused by radiation from massive stars at $\lambda \leq 912$ Å escaping from galaxies and ionizing the surrounding IGM (Finkelstein et al. 2012, 2019; Robertson et al. 2015). Due to the high opacity of the IGM at $z > 6$ to photons just below the Lyman limit, it is difficult to directly observe the fraction of leaking ionizing to non-ionizing radiation in high-redshift galaxies (Vanzella et al. 2012). However, the Lyα feature is well detected out to redshifts near the end of the epoch of reionization (i.e. $z \sim 6$; Stark, Ellis & Ouchi 2011; Schenker et al. 2014; De Barros et al. 2017) and while significantly more challenging, even into the epoch of reionization (e.g. Jung et al. 2018). By modelling the rest-UV spectra of LBGs to infer the intrinsic ionizing luminosity, Steidel et al. (2018) has shown that

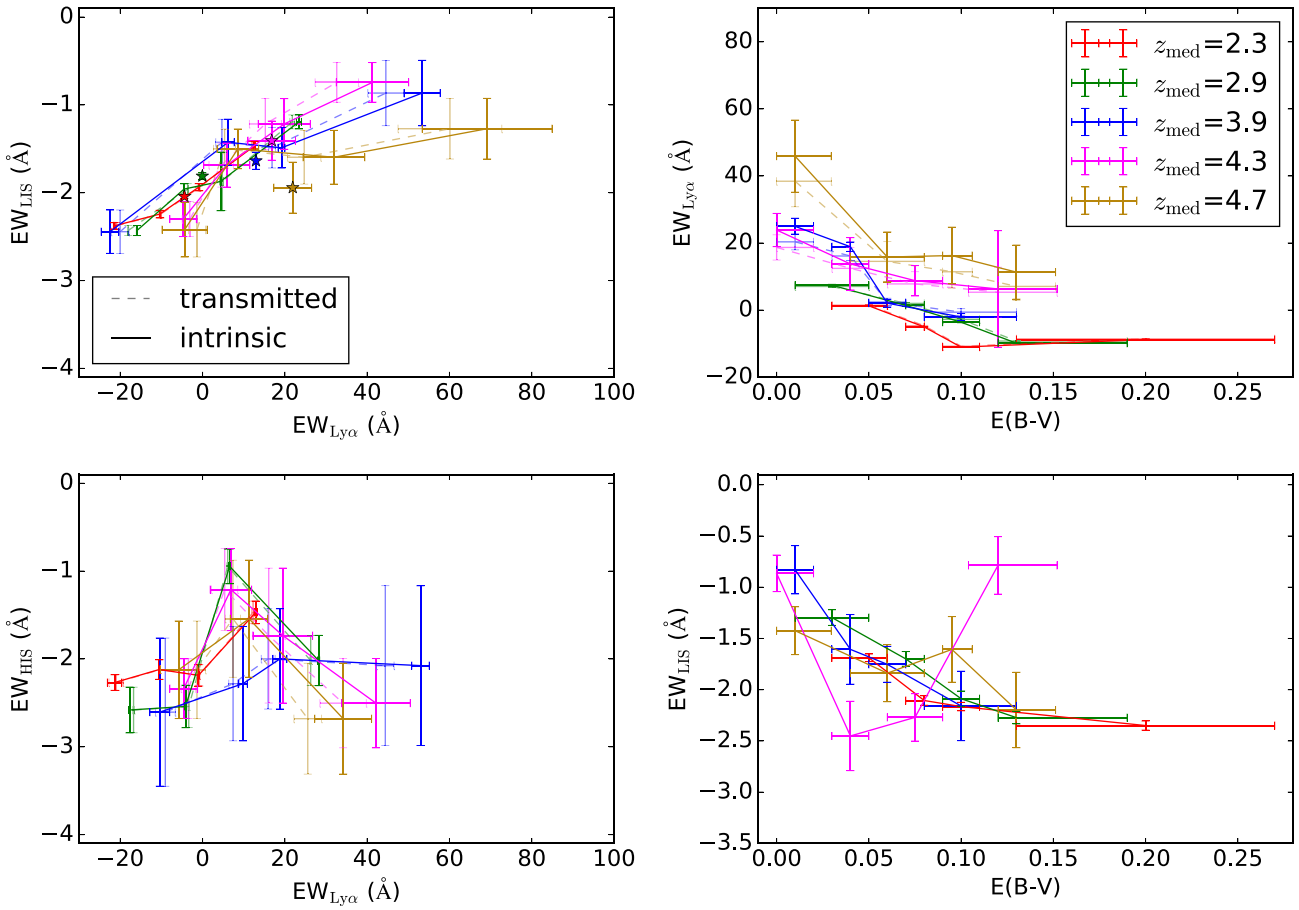

Figure 15. Relations between EW$_{Ly\alpha}$, EW$_{LIS}$, EW$_{HIS}$, and $E(B-V)$ with the two redshift subsamples at $z \sim 5$. The magenta and gold points are the $z \sim 5$ sample divided into a lower and higher redshift sample of $z_{med} = 4.34$ and 4.73. EW$_{Ly\alpha}$, EW$_{LIS}$, and EW$_{HIS}$ were measured from composite spectra. The measurements from the observed composites are displayed in transparent points connected by dotted lines, while the corrected measurements after application of degraded IGM transmission curves are the opaque points connected by solid lines. The red, green, and blue points are measurements of the $z \sim 2$, 3, and 4 samples of D18. *Top left panel:* EW$_{LIS}$ versus EW$_{Ly\alpha}$ with two redshift samples of $z \sim 5$. Each redshift sample was divided into four bins of increasing EW$_{Ly\alpha}$. Both EW$_{Ly\alpha}$ and EW$_{LIS}$ are measured from composite spectra made from combining the individual spectra of the objects in each EW$_{Ly\alpha}$ bin. Also included are average measurements of the composites of the $z \sim 2$–4 samples and the $z_{med} = 4.34$ and 4.73 subsamples, displayed as stars. *Bottom left panel:* EW$_{HIS}$ versus EW$_{Ly\alpha}$. The binned samples are the same as the top panel, with the exception that the objects were required to have coverage of C IV λ1548, 1550. EW$_{HIS}$ and EW$_{Ly\alpha}$ are also measured from composite spectra, made from combining the individual spectra of the objects in each EW$_{Ly\alpha}$ bin. The EW$_{HIS}$-EW$_{Ly\alpha}$ measurement in the highest EW$_{Ly\alpha}$ bin of the $z_{med} = 4.73$ subsample was removed due to contamination from CIV emission. *Top right panel:* EW$_{Ly\alpha}$ versus $E(B-V)$. Each sample was divided into four bins of increasing $E(B-V)$, with EW$_{Ly\alpha}$ measured from composite spectra and $E(B-V)$ from the median of the objects in each bin. The transparent points are individual detections. *Bottom right panel:* EW$_{LIS}$ versus $E(B-V)$. The binned samples are the same as the top panel, with EW$_{LIS}$ also measured from composite spectra.

the fraction of escaping ionizing radiation in a galaxy at $z \sim 3$ is an increasing function of EW$_{Ly\alpha}$. This result supports a physical picture of both Ly α photons and ionizing radiation escaping through 'holes' in the neutral ISM, similar to that discussed in Reddy et al. (2016). This picture is empirically supported the Ly α profile and Lyman continuum emission of Ion2 in Vanzella et al. (2019). Thus, understanding the intrinsic Ly α strength of high-redshift galaxies can provide important clues to the evolution of leaking ionizing radiation, and consequently the epoch of reionization (Jung et al. 2018; Mason et al. 2018; Laursen et al. 2019).

5.1 Splitting $z \sim 5$ sample into low- and high-redshift

Given the size of the $z \sim 5$ sample [including over twice as many galaxies as in the $z \sim 4$ sample from Jones et al. (2012)] and our desire to obtain finer redshift sampling with a high-redshift bin that approaches the epoch of reionization, we isolate high-redshift subsamples within our $z \sim 5$ data set. We divide the $z \sim 5$ sample at its median redshift. Our 'low-redshift' $z \sim 5$ bin contains 87 galaxies with $z_{med} = 4.34$, and our 'high-redshift' $z \sim 5$ bin contains 88 galaxies with $z_{med} = 4.73$.

The strengths of interstellar metal lines and Ly α in the lower- and higher-redshift $z \sim 5$ subsamples are presented in the left panels of Fig. 15. The purple $z \sim 5$ line of Fig. 13 at $z_{med} = 4.52$ is replaced by a magenta curve for the $z_{med} = 4.34$ sample and a gold curve for the $z_{med} = 4.73$ sample. At $z_{med} \leq 4.34$, the positive correlation between EW$_{LIS}$ and EW$_{Ly\alpha}$ is preserved. This unchanging correlation reflects the fundamental connection between the amount of neutral gas and the attenuation of the Ly α line. In the $z_{med} = 4.73$ sample, the trend begins to evolve at EW$_{Ly\alpha} \geq 20$ Å. We observe stronger Ly α emission at fixed LIS absorption strength.

The average properties of the composite spectra out to $z \sim 5$ are displayed as stars in the upper left panel of Fig. 15. At $z_{med} \leq$

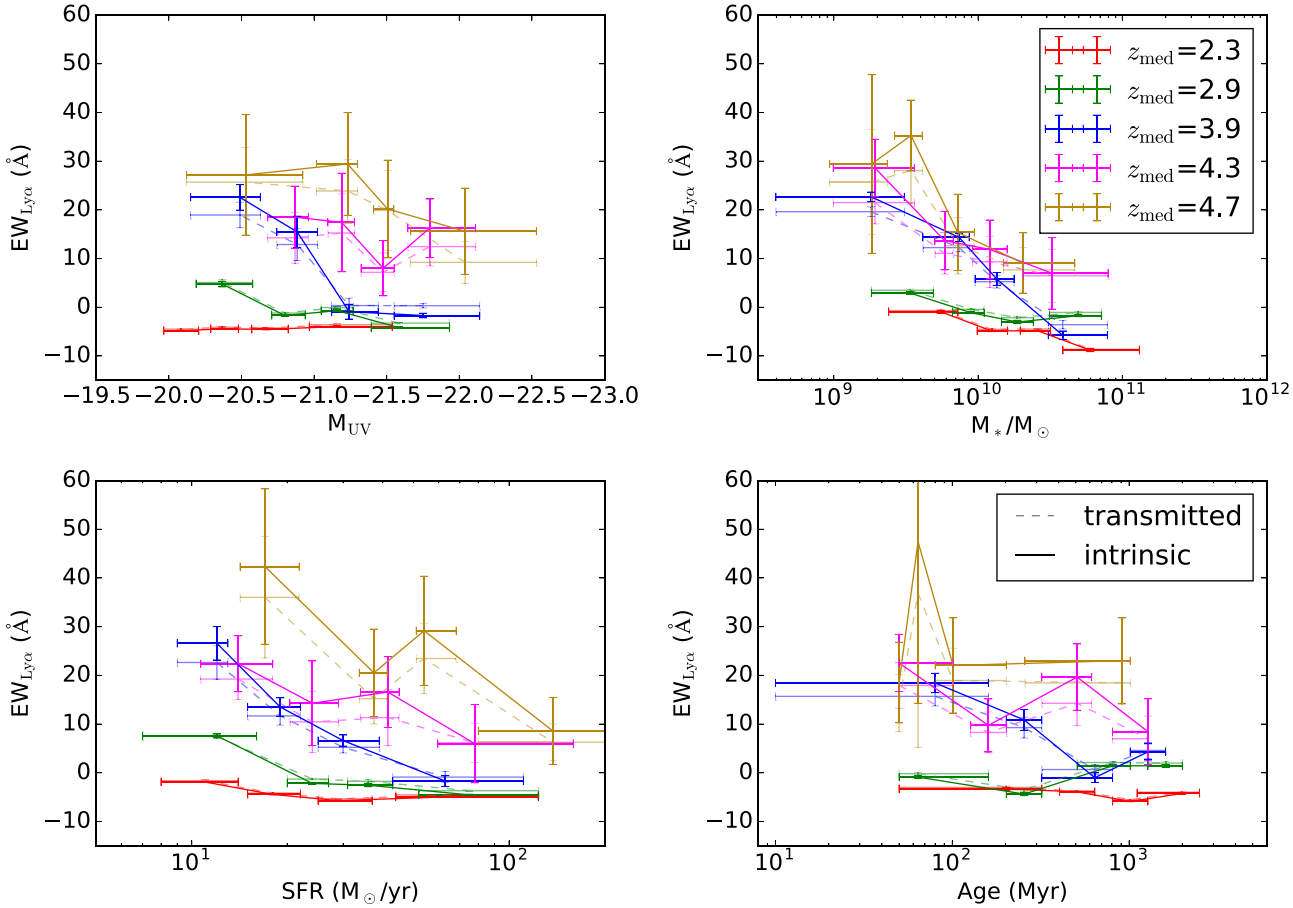

Figure 16. EW$_{Ly\alpha}$ as a function of integrated galaxy properties. The magenta and gold points correspond to the purple points of Fig. 14 split into two redshift samples of $z_{med} = 4.34$ and 4.73. Within each panel, each redshift sample is divided into four bins of an increasing galaxy property corresponding to that displayed on the x-axis: clockwise from top left, M_{UV}, M_*, age, and SFR. The dashed lines connect measurements of EW$_{Ly\alpha}$ from the composite spectra and the median galaxy property of the objects in each bin. The solid lines represent the same measurements after applying the IGM transmission curves of Laursen et al. (2011).

4.34, the average Ly α emission strength increases and the average LIS absorption strength decreases with increasing redshift. This trend indicates that the neutral-gas covering fraction is decreasing with increasing redshift. This relationship appears to be different at $z_{med} = 4.73$, where the average properties of the $z_{med} = 4.73$ sample are offset from the trend of decreasing EW$_{Ly\alpha}$ with increasing EW$_{LIS}$ established at $z_{med} \leq 4.34$. This result implies additional factors beyond neutral-gas covering fraction are influencing the average EW$_{Ly\alpha}$ and EW$_{LIS}$ of the $z_{med} = 4.73$ subsample.

We further probe the state of the ISM near the epoch of reionization based on the mutual relationships among EW$_{Ly\alpha}$, EW$_{LIS}$, and $E(B-V)$. The upper right panel of Fig. 15 shows stronger EW$_{Ly\alpha}$ emission in bluer galaxies, similar to that of Fig. 13, with the two $z \sim 5$ subsamples more clearly illustrating the evolution at $z_{med} \geq 4.34$. Galaxies at $z_{med} \geq 4.34$ have stronger Ly α emission at fixed $E(B-V)$. This evolution is not present in the relationship between EW$_{LIS}$ and $E(B-V)$ shown in the lower right panel of Fig. 15: stronger LIS absorption correlates with more reddening, invariant with redshift.

The redshift evolution of EW$_{Ly\alpha}$ and other galaxy properties of Fig. 14 also sheds light on the physical differences of galaxies as we look back towards the epoch of reionization. The trends found in the single $z \sim 5$ sample analysis are more strongly demonstrated in Fig. 16, based on the lower- and higher-redshift $z \sim 5$ subsamples. The pattern of lower EW$_{Ly\alpha}$ in brighter, more massive, highly star-forming galaxies is preserved across all redshift samples. This trend can also be seen down to $z \sim 0$ (Hayes et al. 2014). Additionally, the evolution towards greater EW$_{Ly\alpha}$ at fixed M_{UV}, SFR, and age with increasing redshift is shown more clearly with the $z_{med} = 4.34$ and $z_{med} = 4.73$ subsamples. While we do not see a correlation of increased EW$_{Ly\alpha}$ with increased specific star formation rate (sSFR), we note that EW$_{Ly\alpha}$ is elevated in the $z_{med} = 4.73$ subsample compared to the $z_{med} = 4.34$ subsample at fixed sSFR, indicating that there are other galaxy properties affecting the strength of Ly α. On the other hand, the relationship between EW$_{Ly\alpha}$ and M_* does not evolve in the three highest redshift subsamples. The trends of EW$_{Ly\alpha}$ and M_{UV}, SFR, sSFR, and age reflect that EW$_{Ly\alpha}$ is increasing at fixed galaxy property, especially at $z_{med} \geq 4.34$. This is similar to the rest-UV spectral trends of Fig. 15, where it is shown that EW$_{Ly\alpha}$ is increasing at fixed ISM/CGM property.

We also detect nebular C IV emission in the highest EW$_{Ly\alpha}$ quartile of the $z_{med} = 4.73$ subsample. This profile, shown in Fig. 17, is similar to that found within the total $z \sim 5$ sample, shown in Fig. 12. We discuss the implications of these detections for the inferred metallicity of the $z \sim 5$ sample in Section 5.3.

5.2 Intrinsic Ly α production evolution

The three factors that affect the observed strength of Ly α in a galaxy spectrum are (1) the intrinsic production rate of Ly α photons in H II

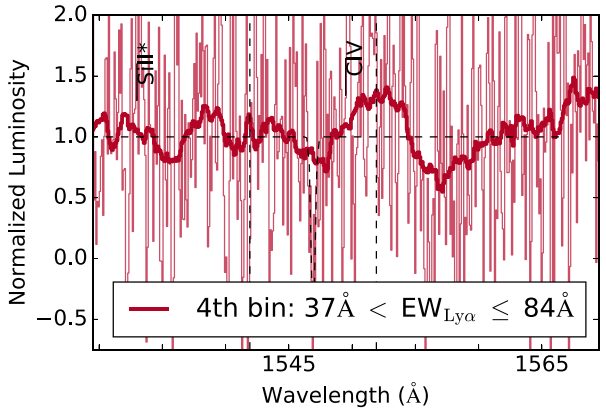

Figure 17. Nebular C IV emission bluewards of the interstellar C IV absorption feature of the $z_{med} = 4.73$ subsample. Displayed is composite of the objects in the highest $EW_{Ly\alpha}$ quartile. As in Fig. 12, the thin curve represents the continuum-normalized, rest-frame composite spectrum. The opaque spectrum is convolved with a boxcar window of width 3 Å for easier viewing. The vertical, dashed lines illustrate the ±5 Å integration windows from which EW measurements would have been made, but due to contamination from the nebular C IV emission, the interstellar C IV measurement was removed from the analysis.

regions, which is set by the efficiency of ionizing photon production for a given SFR, (2) the radiative transfer of Ly α photons through the ISM and CGM of the galaxy, and (3) the transfer of Ly α photons through the IGM. We have corrected for IGM opacity through application of the theoretical transmission curves of Laursen et al. (2011), which, calculated as an average of many sightlines through the IGM, approximate the effects of the IGM on our stacked spectra composed of many galaxies. The anticorrelation between $EW_{Ly\alpha}$ and EW_{LIS}, which remains roughly constant from $z_{med} = 2.3$ to $z_{med} = 4.3$, can be seen as consequence of ISM and CGM radiative transfer. An increased covering fraction of neutral ISM and CGM gas both strengthens LIS absorption and weakens Ly α emission. Based on the lack of evolution in the relationship between $EW_{Ly\alpha}$ and EW_{LIS}, we argue that this correlation is driven by variations in covering fraction of interstellar and circumgalactic gas, and that the intrinsic typical Ly α production efficiency of samples at these redshifts is similar. This is supported by the distinction in Trainor et al. (2019) between quantities related to Ly α *production* and *escape* that jointly modulate observed Ly α strength. The authors argue that EW_{LIS} is strictly an escape-related quantity, supporting our conclusion that changing ISM/CGM properties should entirely define the $EW_{Ly\alpha}$ versus EW_{LIS} relationship assuming intrinsic Ly α production is constant.

The invariance of the $EW_{Ly\alpha}$ versus EW_{LIS} relation breaks down in the highest redshift bin at $z_{med} = 4.73$. In the highest bin of $EW_{Ly\alpha}$, the $z_{med} = 4.73$ sample differs significantly from the relationship defined at lower redshift. Additionally, at $z_{med} = 4.73$, the average $EW_{Ly\alpha}$ and EW_{LIS} deviate strongly from the linear relationship between $EW_{Ly\alpha}$ and EW_{LIS} defined by the lower redshift samples. These deviations, which are at $\geq\sim 1\sigma$, suggest the presence of additional factors modulating the strength of Ly α emission, along with radiative transfer through the ISM, CGM, and IGM. Specifically, this difference suggests a significant increase in the intrinsic efficiency of Ly α photon production, and, correspondingly, ionizing radiation.

A scenario of increased intrinsic Ly α production efficiency among the strongest Ly α emitters at $z_{med} = 4.73$ is additionally favoured by the joint consideration of the $EW_{Ly\alpha}$ versus EW_{LIS} and $EW_{Ly\alpha}$ versus $E(B - V)$ relations. The dust and neutral-gas content in the ISM of a galaxy is intimately connected, with both thought to exist in the same physical location in the galaxy. The relationship between EW_{LIS} and $E(B - V)$ is thus expected to be invariant across redshift, as it is entirely defined by the neutral-gas covering fraction (and consequently the amount of neutral-gas and dust) of the galaxy. The relationship in the bottom right panel of Fig. 15 shows exactly this pattern. On the other hand, the redshift evolution towards stronger Ly α emission at fixed $E(B - V)$ shows that, in addition to the dust and neutral-gas content of the galaxy modulating the strength of Ly α, the intrinsic production rate also increases across redshift (assuming all else being equal). While our results suggest that the dust and neutral-phase gas exist co-spatially, the dust may be present in many locations throughout the ISM/CGM. Fully disentangling the interplay between $EW_{Ly\alpha}$, EW_{LIS}, and $E(B - V)$ will require further work (i.e. individual detections of EW_{LIS}).

The observed difference in intrinsic Ly α photon production rate has important implications for understanding the contribution of galaxies to the reionization of the Universe. The comoving ionizing emissivity of the Universe can be modelled as the cosmic SFR (ρ_{SFR}) multiplied by the number of LyC photons produced per unit SFR (ξ_{ion}) multiplied by the escape fraction of LyC photons from the galaxy (f_{esc}). Physically, the EW of Ly α describes the amount of escaping Ly α emission relative to the non-ionizing UV continuum (analogous to ρ_{SFR} when averaged). The production of these Ly α photons in H II regions comes from recombination of protons and electrons, driven by LyC photons ionizing the hydrogen gas. Given that f_{esc} is directly connected to the properties of the ISM and CGM demonstrated by the relationships of $EW_{Ly\alpha}$, EW_{LIS}, and $E(B - V)$ at low redshift, an evolving $EW_{Ly\alpha}$ at fixed EW_{LIS} and $E(B - V)$ indirectly measures the evolving ξ_{ion} with redshift. The evolution of ξ_{ion} is an important input into models of reionization (Bouwens et al. 2015; Stanway, Eldridge & Becker 2016), and should not be taken as constant (e.g. Robertson et al. 2015).

5.3 Metallicity of the $z \sim 5$ sample

The relationship between UV slope and UV luminosity evolves towards bluer colours at fixed luminosity towards higher redshift (Bouwens et al. 2014). The observed evolution towards decreasing median $E(B - V)$ from $z \sim 2$ to $z \sim 5$ in this work is consistent with these results. This evolution could reflect a fundamental change in dust and metal content of these galaxies, or could reflect a bluer intrinsic stellar population at higher redshift. Spectroscopic observations are required to distinguish among different scenarios of dust, metallicity, or stellar population evolution.

The detection of nebular C IV emission in the highest bin of $EW_{Ly\alpha}$ at $z \sim 5$ provides independent evidence for significantly sub-solar metallicity. Nebular C IV emission is produced by extreme radiation fields in star-forming galaxies (Berg et al. 2019) and detections at lower redshift are typically found in metal-poor galaxies (Erb et al. 2010; Stark et al. 2014; Vanzella et al. 2016, 2017; Senchyna et al. 2017, 2019; Berg et al. 2019). Stark et al. (2015) detected nebular C IV in one galaxy at $z = 7.045$, out of a sample of four $z \sim 6 - 8$ galaxies, whereas the typical C IV detection rate in UV-selected galaxies at $z \sim$ 2–3 is only 1 per cent (Steidel et al. 2002; Hainline et al. 2011). A single, strong C IV detection in a sample of four $z \sim 6 - 8$ galaxies could imply a larger population of lower-metallicity, nebular C IV-emitting galaxies during the epoch of reionization. In our overall $z_{med} = 4.52$ sample, we see strong

nebular C IV emission in the highest $EW_{Ly\alpha}$ bin (near rest-frame 1549 Å in the bottom panel of Fig. 12). In the $z_{med} = 4.73$ subsample, this feature is also prominent, as shown in Fig. 17. A significant detection in a bin containing 25 per cent of the objects in the $z \sim 5$ sample indicates a changing population of galaxies at $z \sim 5$ with greater nebular C IV, harder ionizing fields, and lower metallicity. When compared to the highest $EW_{Ly\alpha}$ quartile of Steidel et al. (2002) at $z \sim 2$, we find an elevated nebular C IV to Ly α flux ratio of 4.0 ± 2.4 per cent and 2.3 ± 1.7 per cent in the $z_{med} = 4.52$ and $z_{med} = 4.73$ samples respectively, compared to $\leq$1 per cent at $z \sim 2$. The EW of this nebular C IV line was measured using the method in Section 3.4 as 1.98 ± 1.13 Å and 1.61 ± 1.08 Å in the $z_{med} = 4.52$ and $z_{med} = 4.73$ samples, respectively.

Systematically lower metallicity in galaxies near the epoch of reionization has important implications for ξ_{ion}. The connection between metallicity and ionizing photon production is more easily studied at lower redshift, where rest-optical metal lines can be observed with ground-based optical telescopes. Shivaei et al. (2018) measured photon production efficiencies in star-forming galaxies at $z \sim 2$ and found galaxies with elevated ξ_{ion} have bluer UV spectral slopes, higher ionization parameters, and lower metallicities. Extreme galaxies at lower redshift with subsolar metallicity have also been demonstrated to have higher average $EW_{Ly\alpha}$ (Erb et al. 2010). These observations at lower redshift paint a physical picture of galaxies with lower metallicity producing an intrinsically harder ionizing spectra per unit SFR, emitting Ly α photons that are also less likely to be absorbed during multiple scatterings in less-dusty ISM/CGM. This picture is once again supported by the framing of Trainor et al. (2019), according to which the evolution of the average $EW_{Ly\alpha}$ versus EW_{LIS} properties across redshift reveals the changing *escape*-related properties of the ISM/CGM, while the evolving metallicity supports changing *production*-related parameters of the stellar population at high redshift. If these lower metallicity, lower neutral-gas covering-fraction galaxies are more common at $z \sim 5$, as suggested by the evolving $E(B - V)$ and nebular C IV emission in our sample, they will contribute more strongly to reionization because of increased ξ_{ion} and f_{esc}. Direct metallicity measurements at $z \geq 5$ are vital to disentangle and quantify these effects.

6 SUMMARY

The rest-UV spectra of star-forming galaxies contain important information on star formation, dust, and metal content of the ISM and CGM, and gas kinematics. Interpreting this information provides clues into the changing galaxy properties closer to the epoch of reionization. These properties include those related to the escape of ionizing radiation, such as neutral-gas covering fraction, and properties related to production of ionizing radiation, such as intrinsic Ly α production rate. To study these properties, we analysed the relative strengths of Ly α, LIS, and HIS lines in a sample of $z \sim 5$ star-forming galaxies for the first time and compared them to similar analyses at $z \sim 2$–4 performed in D18. We also performed corrections for IGM attenuation on the Ly α profiles of sample composites using transmission curves of Laursen et al. (2011). The key results are as follows:

(i) We find that the redshift invariance of the relationship of EW_{LIS} versus $EW_{Ly\alpha}$ deviates at $z_{med} = 4.52$, and even more significantly at $z_{med} = 4.73$, implying an evolving intrinsic Ly α photon production rate at $z \sim 5$ (assuming all else being equal). The EW_{LIS} versus $EW_{Ly\alpha}$ relation illustrates the effects of the neutral-gas covering fraction on the rest-UV spectrum, and greater $EW_{Ly\alpha}$ at fixed EW_{LIS} at $z \sim 5$ implies a greater intrinsic Ly α production rate.

(ii) We find that the relationship of $EW_{Ly\alpha}$ versus $E(B - V)$ evolves at higher redshift, with increased $EW_{Ly\alpha}$ at fixed $E(B - V)$ at $z \sim 5$, but no redshift evolution in the relationship of EW_{LIS} versus $E(B - V)$, suggesting greater intrinsic Ly α production at fixed ISM/CGM properties using the non-evolution of EW_{LIS} and $EW_{Ly\alpha}$ as a control. The invariance of EW_{LIS} versus $E(B - V)$ reflects the fundamental connection between neutral-phase gas content and dust in the ISM and CGM of star-forming galaxies at high redshift. However, we find greater $EW_{Ly\alpha}$ at fixed $E(B - V)$ at $z \sim 5$, implying for a given amount of dust and neutral gas, there are more Ly α photons being produced.

(iii) The robust detection of nebular C IV in the highest quartile of $EW_{Ly\alpha}$ objects within the $z_{med} = 4.52$ and the higher-redshift $z_{med} = 4.73$ subsample supports a scenario of significantly subsolar metallicity in ~25 per cent of our sample of star-forming galaxies near the epoch of reionization. Among non-AGNs, nebular C IV is typically found in a lower-metallicity population in galaxies from $z \sim 0$–2. Additionally, we find evolving UV slopes seen through the changing median $E(B - V)$ from $z \sim 2$–5, also consistent with a more metal-poor population of galaxies at higher-redshift.

(iv) The relationship of EW_{HIS} versus $EW_{Ly\alpha}$ remains invariant with redshift out to $z \sim 5$, implying that ionized-phase and neutral-phase gas in the ISM and CGM remains in physically-distinct regions out to higher redshift.

(v) Higher $EW_{Ly\alpha}$ is correlated with fainter M_{UV}, lower M_*, lower SFR, and younger age at $z \sim 5$, similar to the trends found at $z \sim 4$. We also see an evolution of greater $EW_{Ly\alpha}$ at fixed SFR, M_{UV}, and age at $z \sim 5$. This evolution of greater $EW_{Ly\alpha}$ at fixed galaxy property is consistent with the conclusion that the intrinsic Ly α production rate is increasing at $z \sim 5$.

These results have important implications for the understanding of the evolving galaxy population just after the completion of reionization. Higher intrinsic Ly α photon production rate implies a greater ξ_{ion} at $z \sim 5$, a vital input parameter to models of reionization. The analyses performed here are especially revealing *in* the epoch of reionization, in which the star-forming galaxies are thought to be the most significant contributors to the comoving ionizing emissivity of the Universe. The upcoming launch of the *James Webb Space Telescope*, with its groundbreaking near-IR spectroscopic capabilities, will allow for the measurement of rest-UV spectral features out to $z \sim 10$, and we will discover whether the trends at $z \sim 5$ continue into the epoch of reionization.

ACKNOWLEDGEMENTS

AS, AJP, XD, and MWT acknowledge support for programme GO-15287, provided by the National Aeronautics and Space Administration (NASA) through a grant from the Space Telescope Science Institute (STScI), which is operated by the Association of Universities for Research in Astronomy, Inc., under NASA contract NAS 5-26555. We also acknowledge a NASA contract supporting the 'WFIRST Extragalactic Potential Observations (EXPO) Science Investigation Team' (15-WFIRST15-0004), administered by the Goddard Space Flight Center. We wish to extend special thanks to those of Hawaiian ancestry on whose sacred mountain we are privileged to be guests. Without their generous hospitality, most of the observations presented herein would not have been possible.

REFERENCES

Berg D. A., Chisholm J., Erb D. K., Pogge R., Henry A., Olivier G. M., 2019, ApJ, 878, L3

Berg D. A., Erb D. K., Auger M. W., Pettini M., Brammer G. B., 2018, ApJ, 859, 164
Bouwens R. J., Illingworth G. D., Oesch P. A., Caruana J., Holwerda B., Smit R., Wilkins S., 2015, ApJ, 811, 140
Bouwens R. J. et al., 2014, ApJ, 793, 115
Bouwens R. J. et al., 2016, ApJ, 833, 72
Bruzual G., Charlot S., 2003, MNRAS, 344, 1000
Calzetti D., Armus L., Bohlin R. C., Kinney A. L., Koornneef J., Storchi-Bergmann T., 2000, ApJ, 533, 682
Capak P. et al., 2007, ApJS, 172, 99
Capak P. et al., 2008, VizieR On-line Data Catalog: II/284
Chabrier G., 2003, PASP, 115, 763
Chisholm J., Rigby J. R., Bayliss M., Berg D. A., Dahle H., Gladders M., Sharon K., 2019, ApJ, 882, 182
Chisholm J., Tremonti Christy A., Leitherer C., Chen Y., 2016, MNRAS, 463, 541
Chisholm J. et al., 2018, A&A, 616, A30
De Barros S. et al., 2017, A&A, 608, A123
Du X., Shapley A. E., Martin C. L., Coil A. L., 2016, ApJ, 829, 64
Du X. et al., 2018, ApJ, 860, 75
Erb D. K., Pettini M., Shapley A. E., Steidel C. C., Law D. R., Reddy N. A., 2010, ApJ, 719, 1168
Faisst A. L. et al., 2016, ApJ, 822, 29
Fan X., Carilli C. L., Keating B., 2006, ARA&A, 44, 415
Finkelstein S. L. et al., 2012, ApJ, 758, 93
Finkelstein S. L. et al., 2019, ApJ, 879, 36
Garn T., Best P. N., 2010, MNRAS, 409, 421
Gordon K. D., Clayton G. C., Misselt K. A., Landolt A. U., Wolff M. J., 2003, ApJ, 594, 279
Hainline K. N., Shapley A. E., Greene J. E., Steidel C. C., 2011, ApJ, 733, 31
Hasinger G. et al., 2018, ApJ, 858, 77
Hayes M. et al., 2014, ApJ, 782, 6
Heckman T. M., Alexandroff R. M., Borthakur S., Overzier R., Leitherer C., 2015, ApJ, 809, 147
Jones T., Stark D. P., Ellis R. S., 2012, ApJ, 751, 51
Jung I. et al., 2018, ApJ, 864, 103
Kornei K. A., Shapley A. E., Erb D. K., Steidel C. C., Reddy N. A., Pettini M., Bogosavljević M., 2010, ApJ, 711, 693
Laigle C. et al., 2016, ApJS, 224, 24
Laursen P., Sommer-Larsen J., Milvang-Jensen B., Fynbo J. P. U., Razoumov A. O., 2019, A&A, 627, A84
Laursen P., Sommer-Larsen J., Razoumov A. O., 2011, ApJ, 728, 52
Law D. R., Steidel C. C., Shapley A. E., Nagy S. R., Reddy N. A., Erb D. K., 2012, ApJ, 759, 29
Leitherer C., Otálvaro P. A., Bresolin F., Kudritzki R. P., Lo Faro B., Pauldrach A. W., Pettini M., Rix S. A., 2010, ApJS, 189, 309
Leitherer C., Tremonti C. A., Heckman T. M., Calzetti D., 2011, AJ, 141, 37
Marchi F. et al., 2019, A&A, 631, A19
Mason C. A., Treu T., Dijkstra M., Mesinger A., Trenti M., Pentericci L., de Barros S., Vanzella E., 2018, ApJ, 856, 2
McGreer I. D., Mesinger A., D'Odorico V., 2015, MNRAS, 447, 499
McKinney J. H., Jaskot A. E., Oey M. S., Yun M. S., Dowd T., Lowenthal J. D., 2019, ApJ, 874, 52
McLure R. J. et al., 2018, MNRAS, 476, 3991
Nakajima K., Fletcher T., Ellis R. S., Robertson B. E., Iwata I., 2018, MNRAS, 477, 2098
Oesch P. A. et al., 2013, ApJ, 772, 136
Oke J. B. et al., 1995, PASP, 107, 375
Pentericci L., Grazian A., Fontana A., Salimbeni S., Santini P., De Santis C., Gallozzi S., Giallongo E., 2007, A&A, 471, 433
Pettini M., Rix S. A., Steidel C. C., Adelberger K. L., Hunt M. P., Shapley A. E., 2002, ApJ, 569, 742
Planck Collaboration XIII, 2016, A&A, 594, A13
Reddy N. A., Pettini M., Steidel C. C., Shapley A. E., Erb D. K., Law D. R., 2012, ApJ, 754, 25
Reddy N. A., Steidel C. C., Pettini M., Adelberger K. L., Shapley A. E., Erb D. K., Dickinson M., 2008, ApJS, 175, 48
Reddy N. A., Steidel C. C., Pettini M., Bogosavljević M., Shapley A. E., 2016, ApJ, 828, 108
Reddy N. A. et al., 2018, ApJ, 853, 56
Rix S. A., Pettini M., Leitherer C., Bresolin F., Kudritzki R., Steidel C. C., 2004, ApJ, 615, 98
Robertson B. E., Ellis R. S., Furlanetto S. R., Dunlop J. S., 2015, ApJ, 802, L19
Rudie G. C. et al., 2012, ApJ, 750, 67
Sanders R. L. et al., 2018, ApJ, 858, 99
Schenker M. A., Ellis R. S., Konidaris N. P., Stark D. P., 2014, ApJ, 795, 20
Scoville N. et al., 2007, ApJS, 172, 1
Senchyna P., Stark D. P., Chevallard J., Charlot S., Jones T., Vidal-García A., 2019, MNRAS, 488, 3492
Senchyna P. et al., 2017, MNRAS, 472, 2608
Shapley A. E., Steidel C. C., Pettini M., Adelberger K. L., 2003, ApJ, 588, 65
Shivaei I. et al., 2018, ApJ, 855, 42
Stanway E. R., Eldridge J. J., Becker G. D., 2016, MNRAS, 456, 485
Stark D. P., Ellis R. S., Chiu K., Ouchi M., Bunker A., 2010, MNRAS, 408, 1628
Stark D. P., Ellis R. S., Ouchi M., 2011, ApJ, 728, L2
Stark D. P. et al., 2014, MNRAS, 445, 3200
Stark D. P. et al., 2015, MNRAS, 454, 1393
Steidel C. C., Adelberger K. L., Shapley A. E., Pettini M., Dickinson M., Giavalisco M., 2003, ApJ, 592, 728
Steidel C. C., Bogosavljević M., Shapley A. E., Reddy N. A., Rudie G. C., Pettini M., Trainor R. F., Strom A. L., 2018, ApJ, 869, 123
Steidel C. C., Erb D. K., Shapley A. E., Pettini M., Reddy N., Bogosavljević M., Rudie G. C., Rakic O., 2010, ApJ, 717, 289
Steidel C. C., Hunt M. P., Shapley A. E., Adelberger K. L., Pettini M., Dickinson M., Giavalisco M., 2002, ApJ, 576, 653
Steidel C. C., Shapley A. E., Pettini M., Adelberger K. L., Erb D. K., Reddy N. A., Hunt M. P., 2004, ApJ, 604, 534
Steidel C. C., Strom A. L., Pettini M., Rudie G. C., Reddy N. A., Trainor R. F., 2016, ApJ, 826, 159
Steidel C. C. et al., 2014, ApJ, 795, 165
Strom A. L., Steidel C. C., Rudie G. C., Trainor R. F., Pettini M., Reddy N. A., 2017, ApJ, 836, 164
Trainor R. F., Strom A. L., Steidel C. C., Rudie G. C., Chen Y., Theios R. L., 2019, ApJ, 887, 85
Vanzella E. et al., 2005, A&A, 434, 53
Vanzella E. et al., 2006, A&A, 454, 423
Vanzella E. et al., 2008, A&A, 478, 83
Vanzella E. et al., 2009, ApJ, 695, 1163
Vanzella E. et al., 2012, ApJ, 751, 70
Vanzella E. et al., 2016, ApJ, 821, L27
Vanzella E. et al., 2017, ApJ, 842, 47
Vanzella E. et al., 2019, MNRAS, 483, 3618
Verhamme A., Schaerer D., Atek H., Tapken C., 2008, A&A, 491, 89
Whitaker K. E., Pope A., Cybulski R., Casey C. M., Popping G., Yun M. S., 2017, ApJ, 850, 208

This paper has been typeset from a TEX/LATEX file prepared by the author.